Helically self-organized pinches: dynamical regimes and magnetic chaos healing.

Marco Veranda[1], Daniele Bonfiglio[1], Susanna Cappello[1], Giovanni di Giannatale[1], Dominique Frank Escande[2]

[1]Consorzio RFX (CNR, ENEA, INFN, Università di Padova, Acciaierie Venete SpA) Corso Stati Uniti 4, Padova, Italy
[2]Aix-Marseille Univ, CNRS, PIIM, UMR7345, Marseille, France

E-mail: marco.veranda@igi.cnr.it

Abstract. This paper deals with helical self-organization in current-carrying toroidal pinches for the magnetic confinement of fusion plasmas. We perform our study in the framework of 3D nonlinear visco-resistive magnetofluid modelling, where a large set of simulations is now available. A global picture is derived about how visco-resistive transport coefficients and magnetic boundary conditions rule the self-organized helical states for the reversed-field pinch configuration. Decreasing visco-resistive dissipation causes a transition from steady ohmic helical equilibria to intermittent states (sawtoothing activity), while selected helical magnetic perturbations applied at the boundary favor steady global quasi-helical solutions. The sawtoothing frequency decreases together with visco-resistive dissipation, while sawtoothing amplitude decreases when applying non-resonant magnetic perturbations. Simulations of the tokamak configuration allow us to draw a tight parallelism with reversed-field pinches: a similar role of dissipation and magnetic boundary conditions on the dynamics of the internal kink mode is found, with decreasing sawtoothing frequency and amplitude by decreasing dissipation and by applying suitable helical boundary conditions. Magnetic chaos healing is the topological feature of the transition from intermittent to quasi-quiescent helical states in reversed-field pinches. Bundles of Lagrangian Coherent Structures, LCS, in the weakly stochastic region surrounding the helical core constitute the skeleton of chaos healing, and behave as barriers to the transport of magnetic field lines. In this work, they are detected during the whole temporal evolution and it is proved that they can withstand the nonlinear dynamics even during sawtoothing activity. Furthermore, we show that LCS are connected to regions with strong gradients of the connection length of magnetic field lines to the edge. This provides a further indication of their possible role in the formation of electron temperature barriers. As a final result it is shown that a reasonable value of plasma rotation can further enhance the intensity of the dominant helical mode.

1. Introduction

This paper discusses self-organized helical states in toroidal pinches, and edge magnetic fields as a powerful tool to interact effectively with fusion plasmas. Helical self-organization happens in all high-current toroidal pinch configurations such as tokamaks [1, 2, 3, 4] and reversed-field pinches [5]. It is also observed in nonlinear visco-resistive magnetohydrodynamic (MHD) model. This work focuses on the two key simulation parameters that are most involved in the emergence of 3D quasi-helical states and in mitigating their natural sawtoothing behaviour. Independently from the specific configuration, a first parameter is related to plasma visco-resistive dissipation and defines a transition between stationary helical equilibria and a cyclical dynamics. The other parameter is related to seed helical magnetic boundary conditions and controls the level of intermittency.

The reversed-field pinch (RFP) configuration is the focus of the paper. For this configuration the visco-resistive MHD model predicts that the magnetic field can acquire a helical state in a self-organized manner [6, 7, 8, 9, 10], a feature later observed in high-current plasmas in various RFPs devices (a complete list of RFP devices operating in the world is presented in the end of Sec. 1.1). More recently, the MHD model has predicted new ways for interacting with helical self-organization [11], then validated by experiments [12] in RFX-mod in Padua, Italy.

Modelling of tokamak-like pinches is also addressed with the same MHD model. New simulations are described which show many analogies between tokamaks and RFPs: they have a common intermittent dynamics, associated in the tokamak with the internal kink mode, and they present similar dependence on visco-resistive dissipation and on magnetic boundary conditions, resulting in similar strategies to deal with sawtoothing. A dependence of the sawtooth period with the product of dimensionless resistivity and viscosity is studied, for both tokamaks and RFPs.

This work also discusses magnetic topology and confinement of magnetic field lines in RFP quasi-helical states. The Lagrangian Coherent Structures (LCS) technique is used, borrowed from the study of dynamical systems (for a definition of LCSs see the review papers [13, 14, 15] and the applications in [16, 17]). LCSs allow the discrimination of regions with different transport qualities. In this work, a bundle of resilient LCS are shown to surround the helical core during the whole dynamical evolution of the configuration, reinforcing the magnetic chaos healing effect provided by the formation of perfectly conserved helical magnetic surfaces in the core and safeguarding it, especially during relaxation events. Moreover we show a clear relationship between large gradients in connection length of magnetic field lines to the edge and the presence of LCS - an important clue to their role in the formation of internal transport barriers.

Finally, the paper investigates the role of plasma flow in the emergence of helical states. In fact, we show that macroscopic plasma rotation, with intensity comparable to the experimental ones, can add further beneficial robustness to reversed-field pinch quasi-helical states.

This work is structured as follows: in Sec. 2 we describe the employed MHD model. In Sec. 3 we focus on the pervasive presence of helical states in the solution of the nonlinear magnetohydrodynamics model. In particular, in Sec. 3.1 and 3.2 we describe the dynamical transition to quasi-helical states in the RFP, influenced by viscoresistive dissipation and by helical boundary conditions for the magnetic field. In Sec. 3.3, we describe by numerical simulations with decreasing dissipation the emergence of a RFP helical state with a twist given by helical edge magnetic fields, with the aim of clarifying the key factors involved in the spontaneous emergence of quasi-helical states observed in experiments at high plasma current. In Sec. 3.4, we explain that at high current we can make the helical states more quiescent and tune their amplitude by a suitable choice of the magnetic boundary conditions. In Sec. 3.5 and 3.6 we highlight similarities with basic tokamak simulations.

In Sec. 4, we present the studies about magnetic field line transport in the RFP. There we show how a resilient bundle of Lagrangian Coherent Structures (LCS) can hinder the transport of magnetic field lines and enhance the magnetic chaos healing effect associated with the formation of quasi-helical states, in particular the ones based on non-resonant MHD modes. Finally, in Sec. 5 we describe a result about the role of a mean plasma rotation. In Sec. 6, we draw some final remarks.

In the following short section, we present few historical remarks about helical states in RFPs.

1.1. Historical background

The first theoretical prediction of a helical configuration for the magnetic and plasma current in hot pinches, and in particular in the RFP, was given in the framework of the so-called Taylor's conjecture, which first appeared in the '70s [18, 19]. The core of the conjecture is that, in an isolated and weakly resistive plasma, magnetic energy relaxes to a minimum value, while magnetic helicity is conserved. This "relaxation" theory allows one to: i) obtain a theoretical framework to explain the experimental observation of toroidal field reversal at the edge when the pinch parameter $\Theta > 1.2$ (previously not understood) and ii) predict helically symmetric fields when $\Theta > 1.56$ (see Eq. 6 for a defi-

nition of the pinch parameter Θ).

In the following two decades, theoretical work went beyond Taylor's conjecture and the quasi-helical self-organized nature of the RFP fields became apparent by numerically solving the 3D nonlinear MHD model [20, 6, 8, 21, 9]. Quite a different picture of the emergence of helical states was drawn: they were identified as the nonlinear saturation of a symmetry-breaking MHD instability, directed towards an ohmic equilibrium state, and sustained by an electrostatic dynamo mechanism [22, 23, 24] (a discussion about the validity of Taylor's conjecture can be found in [25]).

Later on [26], qualitative comparison between the numerical solution of the 3D MHD model and the features observed in high-current RFP experiments was reached by allowing a non-ideal boundary condition for the magnetic field. In recent years, the MHD model continued to offer new insights on the behaviour of high-current hot plasmas by predicting the possibility of influencing the twist of the plasma helical self-organization by seed edge helical magnetic field, a prediction confirmed by dedicated experiments [12] in the RFX-mod device, in Padua, Italy [27]. Other experimental facilities in which these topics are studied are the MST device in Madison, USA [28], the KTX device in Hefei, China [29], EXTRAP T2R in Stockholm, Sweden [30] and the RELAX device in Kyoto, Japan [31].

2. Numerical tools to solve the MHD model

The simulations presented here are performed with the SpeCyl code [21], numerically verified against the PIXIE3D code [32] with excellent results [33]. SpeCyl deals with the simple visco-resistive approximation which combines Faraday law, momentum equation (viscous Navier-Stokes) and the single fluid resistive Ohm's law (in Eqs. 1a,1b,1c) to evolve the magnetic $\boldsymbol{B}$ and velocity $\boldsymbol{v}$ fields in time t. Plasma density is assumed to remain uniform and constant, $\rho = 1$. The pressure term is also neglected: this approximation is often used in dealing with macroscopic behaviour of systems characterized by strong current driven activity. This yields a model with two parameters: the dimensionless resistivity η and viscosity ν. The equations, in dimensionless form, are:

$$\frac{\partial \boldsymbol{v}}{\partial t} + \boldsymbol{v}\cdot\nabla\boldsymbol{v} = \boldsymbol{J}\times\boldsymbol{B} + \nu\nabla^2\boldsymbol{v} + \boldsymbol{S}_M, \tag{1a}$$

$$\frac{\partial \boldsymbol{B}}{\partial t} = \nabla\times(\boldsymbol{v}\times\boldsymbol{B} - \eta\boldsymbol{J}) \tag{1b}$$

$$\nabla\times\boldsymbol{B} = \boldsymbol{J} \tag{1c}$$

$$\nabla\cdot\boldsymbol{B} = 0 \tag{1d}$$

Here $\boldsymbol{J}$ represents the dimensionless plasma current density, and $\boldsymbol{S}_M$ represents an ad-hoc momentum source, used in Sec. 5.

Numerical simulations are performed in cylindrical geometry with aspect ratio $R_0/a = 4$, where $a = 1$ is the cylinder radius and the normalization factor for lengths. Periodic boundary conditions are used for the poloidal and axial coordinates $\theta \in [0 : 2\pi], z \in [0 : 2\pi R_0]$, thus allowing a spectral approach. A generic physical quantity $\boldsymbol{Q}(r,\theta,z,t)$ will thus be written as $\boldsymbol{Q}(r,\theta,z,t) = \sum_m \sum_n \boldsymbol{Q}_{m,n}(r,t)\exp i(m\theta + \frac{nz}{R_0})$, with m poloidal wave number and n axial wave number. A wide spectrum of MHD modes validated by previous simulations (see for example [21, 34]) has been used with poloidal wave number $0 \leqslant m \leqslant 4$. In the following, we call *helical magnetic field* with helicity h a magnetic field whose spectrum consists only of the $B_{0,0}$ and of the $B_{m,hm}$ modes. For such helically symmetric solutions a helical flux function χ can be defined by imposing $\nabla\chi\cdot\boldsymbol{B} = 0$. Together with χ we define an effective radius $\rho = \sqrt{\frac{\chi-\chi_{\min}}{\chi_{\max}-\chi_{\min}}}$ and a helical safety factor $q(\rho) = \frac{d\Psi_{tor}(\rho)}{d\Psi_{pol}(\rho)}$: $\Psi_{pol}(\rho)$ and $\Psi_{tor}(\rho)$ represent the poloidal and toroidal flux across a helical flux surface labelled by ρ, and $q(\rho)$ gives the number of toroidal turns that field lines perform for one poloidal turn around the helical magnetic axis.

The relevant time scales of the system are the Alfvén time $\tau_A = a(\mu_0\rho)^{1/2}B_0^{-1}$ with B_0 on axis field (and normalization factor for the magnetic field), the resistive time $\tau_R = \mu_0 a^2\tilde{\sigma_0}$, with $\tilde{\sigma_0} = \tilde{\eta_0}^{-1}$ on-axis electrical conductivity ($\tilde{\sigma_0}$ and $\tilde{\eta_0}$ represent the corresponding dimensional quantities) and the viscous time $\tau_\nu = a^2\tilde{\nu_0}$, with $\tilde{\nu_0}$ on axis kinematic viscosity. We define the Lundquist number $S = \tau_R/\tau_A = aB_0\mu_0^{1/2}\rho^{-1/2}\tilde{\sigma_0} = \eta_0^{-1}$ and the viscous Lundquist number $M = \tau_\nu/\tau_A = av_A\tilde{\nu_0}^{-1} = \nu_0^{-1}$.

An interesting feature of the equations emerges applying a further rescaling of time [10]:

$$t \to \bar{t} = (\eta/\nu)^{1/2}t \tag{2}$$

and thus $\boldsymbol{v} \to \bar{\boldsymbol{v}} = (\nu/\eta)^{1/2}\boldsymbol{v}$. In this form the equations can be rewritten in terms of two new dimensionless parameters, the magnetic Prandtl number $P = \tau_R/\tau_\nu = S/M$ and the Hartmann number $H = (\tau_R\tau_\nu)^{1/2}/\tau_A = (SM)^{1/2}$ (inversely proportional to visco-resistive dissipation):

$$P^{-1}\left[\frac{\partial\bar{\boldsymbol{v}}}{\partial\bar{t}} + \bar{\boldsymbol{v}}\cdot\nabla\bar{\boldsymbol{v}}\right] = \boldsymbol{J}\times\boldsymbol{B} + H^{-1}\nabla^2\bar{\boldsymbol{v}} + \boldsymbol{S}_M, \tag{3a}$$

$$\frac{\partial\boldsymbol{B}}{\partial\bar{t}} = \nabla\times(\bar{\boldsymbol{v}}\times\boldsymbol{B} - H^{-1}\boldsymbol{J}). \tag{3b}$$

Such new parameters help categorizing in a simpler way the different dynamical behaviors of the system, as will be seen in Sec. 3.6. In particular, when the inertia term is negligible and/or the Prandtl number is large, the Hartmann number turns out to be the only parameter ruling the MHD dynamics.

Dissipation parameters are not evolved in time and are radially parametrized as follows. The dimensionless resistivity η is increased towards the edge to mimic a decreasing plasma temperature (in a fusion plasma, according to Spitzer, $\tilde{\eta} \propto T^{-3/2}$). In the simulations presented in this paper we used $\eta(r/a) = \eta_0(1+20(r/a)^{10})$, with the caveat that different profiles might produce quantitative differences in the resulting simulations (see for example [35]), without changing the general picture about helical states in the solution of the model. Viscosity is kept uniform $\nu(r/a) = \nu_0$, though we plan to address a study of how to better characterize it in the near future, considering recent studies like [36, 37]. For a partial discussion of the topic of transport coefficients, in Appendix A, the characterization of quantities like resistivity and viscosity is given in the framework of fluid theory, as already presented in [38].

Magnetic boundary conditions are defined as follows. The edge radial magnetic field is either zero (the so-called "ideal conducting wall"), or helically modulated through a Magnetic Perturbation (MP) with poloidal and toroidal wave number given by (m_{MP}, n_{MP}). Edge MP is imposed at $r = a$ with amplitude given by the quantity MP%$= B_r(a)^{m_{MP},n_{MP}}/B_\theta(a)\%$ as a single helical modulation of the radial component of the field given by $B_r(a,\theta,z) = B_r(a)^{m_{MP},n_{MP}} \exp i(m_{MP}\theta + \frac{n_{MP}}{R_0}z)$. MPs are imposed at the beginning of the simulation, by adding to the equilibrium magnetic field a vacuum field obtained by solving the stationary form of Eqs.1a with $\boldsymbol{J} = \boldsymbol{v} = \boldsymbol{S}_M = 0$:

$$\nabla \times \boldsymbol{B} = 0, \qquad \nabla \cdot \boldsymbol{B} = 0, \tag{4}$$

and the helical boundary conditions. The resulting profile of the axial component of the magnetic field in the Fourier space is given by:

$$b_z^{m_{MP},n_{MP}}(r) = \varepsilon I_{m_{MP}}\left(\frac{n_{MP}}{R_0}r\right) \tag{5}$$

with $I_{m_{MP}}$ representing the modified Bessel functions of the first kind. The other two components result from Eqs. 4: $ib_r^{m_{MP},n_{MP}}(r) = \frac{R_0}{n}\partial_r\left(b_z^{m_{MP},n_{MP}}(r)\right)$ and $b_\theta^{m_{MP},n_{MP}}(r) = \frac{m_{MP}R_0}{n_{MP}r}b_z^{m_{MP},n_{MP}}(r)$. The quantity ε is a parameter chosen so that MP% has the desired value.

An ad-hoc momentum source $\boldsymbol{S}_M$ can be added to the momentum equation 1a to generate mean flow. In this work some cases adopt the choice $\boldsymbol{S}_M = S_M\hat{\boldsymbol{z}}$, with constant S_M, to test the impact of a momentum source. The aim of the present study is to build up the global picture resulting from a now available extended set of simulations. We remark that the approximations here adopted have been used in several different studies offering useful insights about the major physical effects observed in RFP experiments, confirming a strongly current-driven nature of MHD instabilities in the RFP [39, 40, 41, 42]. Further effects should be considered, which may improve the quantitative comparison with the extremely rich dynamics of experimental devices, such as finite-β, two-fluid effects or the ones associated with toroidal geometry and with fast ion: in Refs. [43, 44, 45, 46] they lead to similar macroscopic dynamics, though quantitative differences can be present.

2.1. 1D equilibrium

The simulations start from an axisymmetric unstable ohmic equilibrium, of the kind described in Ref. [47]. An uniform induction electric field $\boldsymbol{E} = E_0\hat{\boldsymbol{z}}$ is imposed to sustain the plasma current, with E_0/η_0 as the fundamental parameter characterizing different equilibria. Another important parameter is the pinch parameter

$$\Theta = \frac{B_\theta(a)}{\langle B_z\rangle}, \tag{6}$$

which represents the ratio between plasma current and mean toroidal magnetic field used to confine the plasma.

Fig. 1 presents the main features of ohmic axisymmetric equilibria for RFP (first row) and tokamak cases (second row). In the first row of Fig. 1 RFP initial equilibrium quantities are plotted in full lines ($E_0/\eta_0 = 4.2$, $\Theta \sim 1.6$). After the unstable equilibrium is perturbed at the beginning of the simulation, the 3D dynamics provides the so-called RFP dynamo relaxation, leading to a reversed edge axial component of the magnetic field (dotted lines). The basic tokamak simulations considered have $\Theta \sim 0.06$, $E_0/\eta_0 = 0.625$, and a resistivity profile parametrized by $\eta(r/a) = \eta_0(1 + 25(r/a)^4)^{1.5}$: these choices uniquely determine a ohmic axisymmetric equilibrium, unstable to the internal kink mode with m=1, n=1 (the chosen profile correspond to the "rounded model" for current density distributions in Eq. 8 of [48]). The features of tokamak equilibrium are presented in the second row of Fig. 1.

Let us consider Eq. 1a for the velocity field in equilibrium condition:

$$\boldsymbol{v}\cdot\nabla\boldsymbol{v} = \boldsymbol{J}\times\boldsymbol{B} + \nu\nabla^2\boldsymbol{v} + \boldsymbol{S}_M. \tag{7}$$

Since the inertial term is proportional to η^2 through Ohms law, and is therefore negligible [47], the $\boldsymbol{J}\times\boldsymbol{B}$ equilibrium term decouples from the velocity terms. One then gets to balance the viscous dissipation ($\nabla^2\boldsymbol{v}$ term) and the constant momentum source term ($S_M\hat{\boldsymbol{z}}$ term) which results in a parabolic profile of the axial component of the velocity $v_z(r/a) = -\frac{S_M}{4\nu}\left((r/a)^2 - 1\right)$. The parameter $\frac{S_M}{\nu}$ turns out to be the one governing the amplitude of the resulting mean plasma flow.

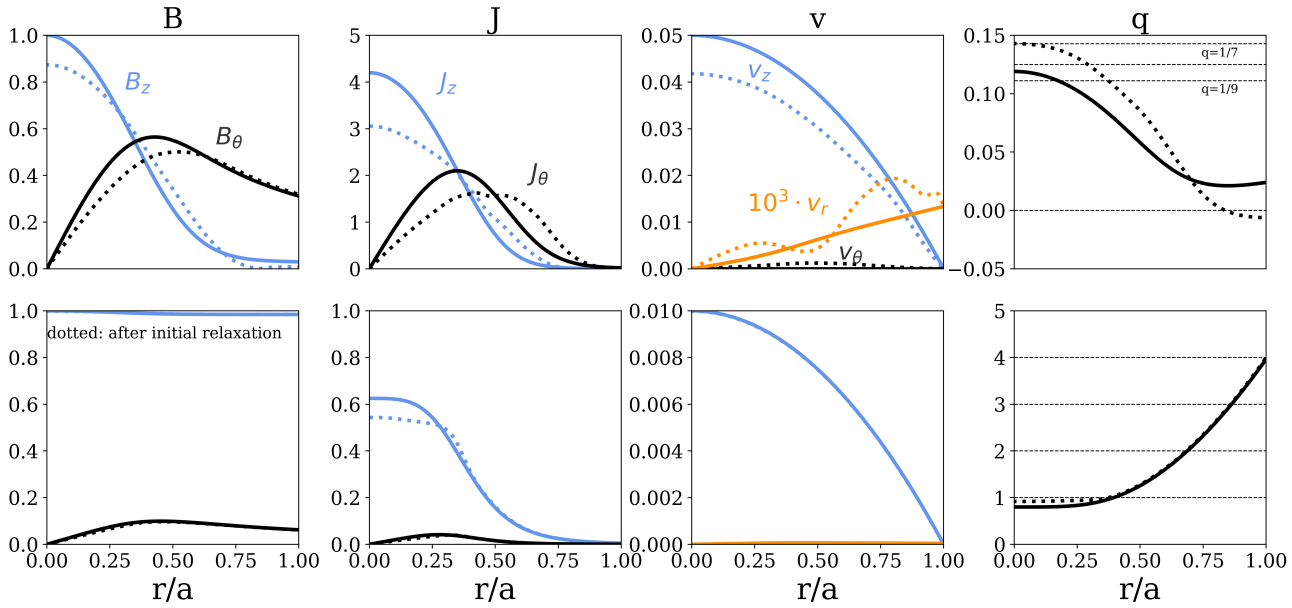

Figure 1. Radial profiles of the equilibrium magnetic, current density and velocity fields in the RFP cases (top row) and in the tokamak cases (bottom row). The B_z component of the RFP magnetic field slightly reverses at the edge, giving the name to the configuration. When a radially constant momentum source is imposed the v_z component of the velocity (third column) has a parabolic profile which gets modified by interaction with the magnetic field, see Sec.5. Magnetic field is normalized to its on-axis initial value, velocity field is normalized to the corresponding Alfvèn velocity. Dotted lines represent the same quantities after the relaxation event following a slight perturbation of the initial equilibrium, resulting in the beginning of the 3D MHD dynamics. In this picture the modulus of all the quantities is plotted.

3. Quasi-Helical solutions of the visco-resistive MHD model

In this section, we describe the results of an extended set of simulations of the visco-resistive MHD model described in Sec. 2. The resulting global picture extends our previous results, consolidating the importance of the Hartmann number and the key role played by edge magnetic perturbations in ruling the helical self-organization process.

A short outline of our results is:

i) several features of the helical regimes are found to be ruled by two quantities only, the Hartmann number and magnetic boundary conditions (seed resonant or non-resonant MPs);

ii) an increase of Hartmann number produces a transition towards a "sawtoothing" behaviour in the dynamics of the magnetic field;

iii) a proper choice of MPs paces the "sawtoothing" dynamics and stimulates quasi-helical states in between sawteeth.

In the following we will describe such theoretical findings in detail, and how they resonate with experimental observations, in particular for helical regimes in the reversed-field pinch configuration. We will show that similar rules are valid also for basic tokamak simulations of m=1,n=1 sawtoothing, within the limits described in the introduction.

This section is structured as follows: at the beginning we describe the dynamics of couples of RFP simulations, choosing "extreme" values of the important quantities, Hartmann number and MP amplitude (Sec. 3.1). Such examples represent the possible qualitative behaviour obtained when spanning the simulations "parameter space". Then, quantitative results will be shown for a larger number of simulations, analyzing the energy associated with the dominant helical mode versus the energy of the other MHD modes, an indicator of the "spectral purity" of the helical solution, often used also in experimental analyses (Sec. 3.2). Finally two additional examples will be presented, showing how the MHD modelling connects with experiments.On the first the focus will be on showing how helical regimes are strongly favoured at high Hartmann number/low dissipation (Sec. 3.3) when suitable tiny helical perturbations are present. The second example focuses on the effect of helical boundary conditions (Sec. 3.4) showing that non-resonant edge MPs tend to pace the sawtoothing dynamics.

Then, by discussing a number of new 3D simulations of tokamak type involving the dynamics of the internal kink mode analogies between RFP and tokamak cases will be discussed (Sec. 3.5). As a final part, the pulsation time of the sawtoothing events observed in numerical simulations of both the tokamak and of the RFP is characterized, showing that it can be simply

described using the Hartmann number (Sec. 3.6).

3.1. RFP helical regimes

In the reversed-field pinch configuration the features of helical dynamical regimes undergo a transition which is ruled only by two quantities, visco-resistive dissipation (Hartmann number) and boundary conditions for the magnetic field. We start by considering a magnetic perturbation applied on the m=1, n=-7 mode, which correspond to the helical twist typically observed in RFX-mod operation at high current. We first show in Fig. 2 the four different regimes which can be obtained making "extreme" choices for these two quantities.
In Fig. 2 we plot the temporal evolution of the total energy (volume integral) associated to the most important m=1 helical modes. Consider the helical states found at low Hartmann number and zero MP (top left): at $t \sim 0.1\tau_R$ the stationary helical solution of the model is made up of a single MHD mode with m=1, n=-11 (SH Single Helicity states, with well-defined magnetic surfaces in the whole plasma volume). This mode is different from the most unstable ones, which at the very beginning of the simulation around $t \sim 0.02\tau_R$ create a 3D sequence of modes with increasing periodicity number starting from n=-7, sequence that is typical of the RFP multiple helicity relaxations. However, at a certain time, the (1,-11) mode overcomes the competition with the others and absorbs the energy from the other secondary modes, which exponentially decay to vanishing amplitude. At high values of H and zero MP (top right) instead, a strong competition between MHD modes ends in the presence of a pulsating regime (MH Multiple Helicity states, with stochastic magnetic field lines) intermittently featuring discrete reconnection events [34], for example at $t \sim 0.035\tau_R$. In particular, one notices that the energy associated to the modes is two orders of magnitude lower in the high H cases, where it reaches values compatible with experimental measurements in the RFX-mod device.
In the second row of Fig. 2, we turn on the helical boundary condition on the m=1, n=-7 mode with amplitude MP%= 2%. In the low H and MP-on quarter (bottom left) we observe that the system reacts to the new boundary condition by amplifying to large amplitude the one stimulated by MPs in the spectrum of helical modes. In the end the m=1, n=-11 mode remains the most energetic one, while the m=1, n=-7 mode remains stationary at a finite energy. Topologically, the final state of the bottom left panel corresponds to a MH state, with stochastic magnetic field lines. Additional simulation cases not presented here, showed that helical states with different dominant helicities are possible in highly dissipative regimes, provided a high-enough MP amplitude is applied (the threshold is around 10% with this value of dissipation). Finally, in the high H and MP-on quarter (bottom right) we find a systematic repetition of quasi-helical states, with a clearly dominating MHD mode which has the same twist of the applied MPs, creating conserved magnetic surfaces in the core, studied in Sec.4. Thus, in the end, the applied MP is successful in overcoming the other modes thanks to the natural depression at higher H values of the competing modes. This last example is the most adherent to the experimental observations in RFX-mod, as was discussed in [26]. In Ref. [12] another prediction was made, later experimentally verified: MPs with different helical twist stimulate a QSH state with their helical pitch.

3.2. Extended analysis of numerical cases

We make the considerations of the previous sections more quantitative by computing the time average of the magnetic energy associated to the various MHD modes involved in the dynamics. We consider a wide set of approximately 100 MHD simulations with varying (S, M, MP%, n_{MP}). We will show the results of a subset of simulations with $n_{MP} = -7$: similar results are obtained considering helical regimes with helicities close to this one.

Two requirements must be met in order to diagnose the presence of a QSH or of a SH state:
i) large positive difference between the magnetic energy of the dominant m=1 mode and the sum of the energy of other m=1 modes, indicating the presence of a helical structure. The limit case corresponds to the absence of m=1 secondary modes (SH);
ii) low magnetic energy of the m=0 MHD modes, indicating a low level of nonlinear interaction between the m=1 modes (another symptom of the presence of a dominant helical mode and of the absence of secondary modes).
Panel a) of Fig. 3 showing the volume energy of m=1 modes for a set of MHD simulations *without MPs* and with varying dissipation (each point corresponds to time-averages of one simulation). We find a positive energy difference between the dominant mode (pink full circles in panel a) and the secondary modes (pink empty circles) only at very low values of H (condition i). If we check the condition ii) (look at pink pentagons in panel c) we observe that the energy of m=0 modes decreases at low Hartmann number. Thus, without MP long-lasting QSH state can be found only at low values of H (for the temporal dynamics look at the top-left panel of Fig. 2). Such states were deeply studied in the past, for example in Refs. [7, 10]. In particular it was shown that the dominant helicity in highly dissipative regimes without MPs depends on the value of Θ [34].

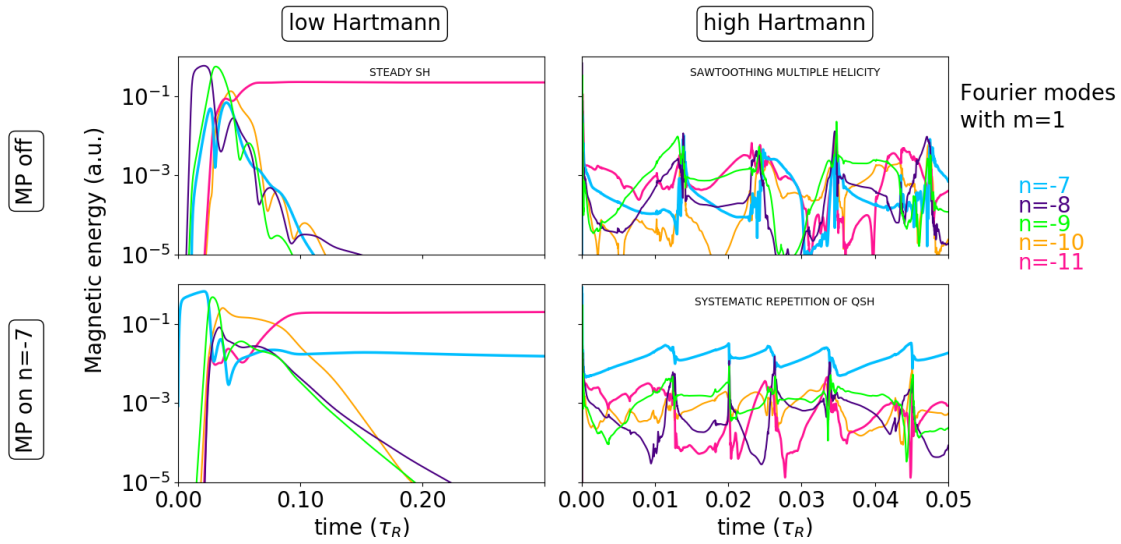

Figure 2. Solutions of the 3D nonlinear MHD model for RFP cases. Helical states are found at low Hartmann number (top-left) characterized by a 2D symmetry (SH Single Helicity states, with well-defined magnetic surfaces in the whole plasma volume). In the bottom-right corner, corresponding to high values of H and using MPs, we find a state with a high level of helical symmetry (with the same twist of the MPs).

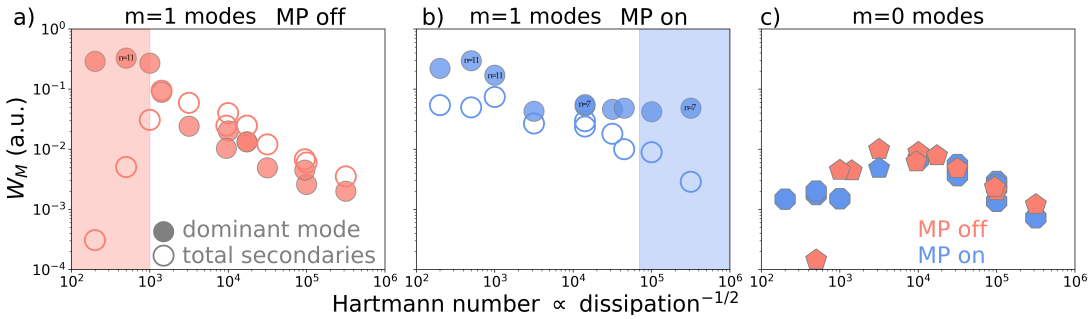

Figure 3. Two shaded regions where QSH states can be predicted by 3D nonlinear visco-resistive MHD modelling: a pink one at very high dissipation (panel a), with spontaneous 2D helical states, and a blue one at low dissipation only when MPs are turned on (panel b). The toroidal mode number of the dominant mode is indicated inside some full circles. The behaviour of m=0 MHD modes, to be compared with previous results in [34] also confirm the presence of these two regions. Intermediate regions ($H \sim 10^3$) instead do not correspond to helical solutions.

The scaling of the secondary modes' amplitude in the first panel of Fig. 3 changes abruptly around $H_c \sim 3 \cdot 10^3$: this is the signature of a dynamical transition. In the region $H < H_c$ the scaling is $W^{m=1}_{M,sec} \propto H^{3.1}$, calling for a reduction of the Hartmann number to access helical states at very high plasma dissipation (meaning low plasma current and/or high plasma density). In the region $H > H_c$ the scaling is $W^{m=1}_{M,sec} \propto H^{-0.6}$, calling for an increase of Hartmann number to reduce fluctuations (meaning high plasma current and/or low plasma density).

Let us then consider the panel b) (blue dots) of Fig. 3, corresponding to a set of MHD simulations *with MPs* on the m=1 n=-7 MHD mode with amplitude MP%∼4% (such a value is chosen to facilitate the emergence of QSH states, which occurs even with the smaller intensity MP%∼2%) and with varying dissipation. If we check the condition i) we find a positive energy difference between the dominant mode (blue full circles in panel b) and the secondary modes (blue empty circles) only at high Hartmann number. At low Hartmann number the mode stimulated by the MPs does not become the dominant one and its role is that of perturbing the "no-MP" helical regime creating a state with two dominant helicities, like in the bottom-left corner of Fig. 2. This is confirmed by checking the condition ii) (look at blue octagons in panel c) showing the saturation of the amplitude of the m=0 modes at low H. Instead, we observe a clear decreasing trend of the energy of m=0 modes only at high Hartmann number: this feature, together with the presence of a single dominant m=1 mode (full blue dots in panel b),

characterizes the Quasi-Single Helicity states (like the one in the bottom right corner of Fig. 2).
Thus there are two regions where long-lasting QSH regimes, i.e. obeying to the two requirements written before, can be found. Pure and robust and stationary helical regimes are present at $H \ll H_c$ and are studied in [7, 10, 34], where the features of the intermediate turbulent regimes found at $H \sim H_c$ are also described. The regimes detected at $H \gg H_c$ display the typical intermittent behaviour observed in RFP experiments. They were studied in [26, 11].
Though the low-H regimes would represent a stationary, stochasticity-free option for the operation of an RFP device, comparison with experimental results tends to rule out the high-dissipation solution. In fact a reasonable lower bound for the Hartmann number value in typical RFX-mod experiments is $H > 10^5$ (see Ref. [38] for an estimate of H in RFX-mod).
In summary, the extended numerical study presented in this subsection provides a complete picture of the different helical regimes of the RFP and of the transition between them. The major conclusion is that there is just one region where long-lasting QSH state qualitatively similar to experimental observations can be found, i.e. only at high Hartmann number and only using MPs with the proper amplitude.

3.3. Role of low dissipation in favoring QSH emergence

As a confirmation of the results presented in the previous section, here we show additional numerical results to highlight how QSH states are observed only under a threshold in plasma dissipation. As shown above, low dissipation favors the externally stimulated mode by damping the other modes amplitude: this allows the mode stimulated by the MPs to overcome the competition, build up a quasi-helical state and heal magnetic chaos, as we shall see on the next Sec. 4. The phenomenon of "QSH emergence at high current / low dissipation" is observed in RFX-mod experiments (see Fig.5 of [49]), where QSH states are measured over a threshold in plasma current and below a threshold in plasma density. We describe a simulation where we decrease plasma dissipation (increase Hartmann number) every 0.2 τ_R while imposing a stationary, low amplitude, MP. This is a paradigmatic example of "emergence of a QSH state at low dissipation/high current", which resonates with experimental findings. Indeed, in the experiments the dominant helicity and radial magnetic field amplitude at the edge (which is usually different from zero see Fig. 3 in Ref. [50]) result from the spontaneous self-organization of the whole system constituted by plasma and magnetic front-end (resistive shell, vacuum layer and a rich system of coils for feedback interaction and/or control). In the standard operations, the feedback system tries to nullify the radial magnetic field while in other cases a finite suitable helical MP is applied on purpose. Thus, our simulations (featuring an ideal wall at the plasma and a fixed constant MP) should be considered a very schematic representation of the real system. An upgrade of the magnetic boundary condition in simulation was recently presented in Ref. [51]. In the following simulation, we keep the ratio between viscosity and resistivity fixed ($P = \nu/\eta = 10^2$, with $\eta \in [10^{-7} : 10^{-4}]$ and $\nu \in [10^{-5} : 10^{-2}]$). A stationary helical MP is imposed with amplitude $MP\% = 2\%$ on the non-resonant MHD mode with $m_{MP} = 1, n_{MP} = -6$. This represents a difference with the experiments, where helicity and radial field amplitude at the edge, result from the self-organization (except for cases in which the radial component is forced by the control system). The result of Fig. 4 does not depend on the helicity of the QSH, as long as it remains in the range $-5 \leq n_{MP} \leq -10$, as described in Sec. 3.4. Fig. 4 shows in blue the temporal evolution of the magnetic energy associated with the mode "stimulated by the MPs" (m=1, n=-6), while in black we plot the sum of the magnetic energy associated with the other m=1 modes. We start at $t = 0$ from a low value of $H = 10^3$. In this highly dissipative regime, the m=1, n=-11 mode dominates the spectrum and the MHD mode with the same twist of the MP does not emerge as the dominant one (blue line is below the black one). Increasing H at $H = 2.5 \cdot 10^3$ allows the n=-6 mode recovering a little more energy while the energy associated with the other MHD modes starts decreasing. We observe the appearance of intermittency: such cycles are characterized by a temporary QSH formation (when the blue line is higher than the black one we have the first evidence of a m=1, n=-6 QSH state) and are commonly observed in experiments (see, for example. Fig.2 of [49]). When we exceed a threshold around $H \sim 4 \cdot 10^3$, in the time interval between $0.4\tau_R \leq t \leq 0.8\tau_R$, we observe an increased temporal intermittency of the helical field, qualitatively similar to the ones most often observed in RFX-mod experiments for plasma currents around 1.5MA with hydrogen as main gas. The study of the dynamics at $H = 10^5$, which may well be inside the presently explored values in RFX-mod, indicates the possibility of a more persistent and quiescent helical state, with strongly reduced perturbations' intensity (compare the final part of the simulation with RFX-mod data in Fig.9 of [52]). We find that the intensity of the perturbations decreases following the scaling $b_{pert} \sim H^{-0.3}$ (see Fig.3). Scaling laws from fluid plasma transport theory indicate that the Hartmann number is proportional to plasma temperature T (and thus to plasma current I_P) and to the inverse of plasma

density n, $H \sim Tn^{-1}$ [38]: this clearly resonates with QSH emergence only over a threshold in plasma current and under a threshold in plasma density.

3.4. Role of Magnetic Perturbations in mitigating oscillatory dynamics

MPs represent a useful mean to mitigate/pace the intermittency often associated with quasi-helical states formation. We now show that imposing MPs with a twist non resonant with the safety factor profile (see Fig. 1) can make the quasi-helical configuration more quiescent than in the usual resonant cases. We describe this behavior in Fig. 5a): we show the temporal behavior of the mode stimulated by the MPs in three different simulations. In the first, in light blue, we impose MPs on the $m_{MP} = 1$, $n_{MP} = -9$ MHD mode with amplitude MP%= 2% and we note that the amplitude of the axial component of the mode $b_z^{1,-9}$ spans normalized values between 4% and 14% during its temporal evolution, with a quasi-periodic cycling. The second time trace is related to a simulation with MPs on the resonant $(1, -7)$ mode, always with the same MP%= 2%: here we note a minor excursion in $b_z^{1,-7}$ and a slightly lower frequency of QSH breakdown events. The third time trace instead shows an example of the pacing effect of a non-resonant MP: we made a simulation imposing MPs on the non-resonant (1, - 5) MHD mode and we note that the temporal behavior of the magnetic field is more quiescent than in the other cases, with a much minor $b_z^{1,-5}$ amplitude span. All these results can be synthetized in panel b) of Fig. 5. The big-dots indicate that non-resonant modes ($n_{MP} >= -6$) are characterized by a less intense response of the plasma to the applied MP and by a less wide amplitude span (indicated by the shaded region) meaning an increased quiescence. As for the resonant ones ($n_{MP} <= -7$) we find that the most intense reaction to the imposed MP is around $n_{MP} = -9$, quickly fading away as n_{MP} deviates from this value: in fact, analyzing the simulations with $n_{MP} = -11$ one notices that the amplitude of the dominant (resonant) mode is equal to the one associated to the (non-resonant) $n_{MP} = -5$, though with much wider amplitude span (indicating intermittency). We also describe the amplitude of m = 1 secondary modes with the little dots, which show a structure similar to that of the dominant helical mode. Summarizing, while plasma responds less to non-resonant MPs (according to Fig. 5, panel a) the temporal evolution is more quiescent than in the resonant case, with rarer QSH-breakdown events characterized by a lower drop of amplitude of the dominant MHD mode: building QSH states upon non-resonant modes (so-called Resistive Wall Modes [53]) allows obtaining a more quiescent dynamics [12].

3.5. Analogous tokamak simulations

This part is devoted to tokamak simulations in the framework of the same 3D visco-resistive MHD model, with the aim of drawing analogies with the RFP behavior analyzed in the previous part. Sawtoothing solutions can be obtained with the visco-resistive MHD model we are using, as already presented in Refs.[54, 55, 56], despite the simplicity of the model which does not take into account physical effects like heat transport, finite-β or two-fluid effects or those related to toroidal geometry and fast ions: such approximated model is already capable of providing a basic comprehension of experimental observations. Literature about tokamak sawtooth is vast, consider the analytical works of Ref. [57] and references therein and the numerical works in Refs [58, 59, 60, 61, 62]). Sawtooth is known to prevent impurity accumulations in the core region [63] but also to lead to neoclassical tearing modes onset [64]. A set of 3D numerical simulations of the internal kink mode dynamics with our visco-resistive modelling has been performed varying plasma dissipation and MPs' features like in the previous RFP cases. All simulations start from the tokamak equilibrium described in section 2.1.

Fig. 6 has a matrix structure analogous to that of Fig. 2 (dissipation is varied in the horizontal direction, MPs' amplitude in the vertical). Let us look at the simulations on the top row, the ones with no applied MPs. In the tokamak case, high Hartmann/low dissipation (top-right panel) favors the oscillatory dynamics, with the on-axis safety factor periodically crossing the q=1 value and thus triggering the sawtoothing dynamics of the internal kink mode, whose energy oscillates in the range $10^{-7} \leq W_M \leq 10^{-3}$. The low Hartmann/high dissipation simulations on the top-left panel exhibit a stationary behaviour. The dissipation parameters are $S = 10^4$ and $M = 10^4$ ($H = 10^4, P = 1$) for the high-dissipation case, while the low-dissipation case in the top-right has $S = 10^6$ and $M = 10^3$ ($H = 3.16 \cdot 10^4, P = 10^3$).

The bottom row shows the effect of a MPs on the m=1, n=-1 mode dynamics (other details on the simulations can be found in [55], Fig.3, 4). An analogy with the RFP is that a proper amount of MP amplitude (MP%= 1.5% in this case, or the 0.1% of the total field at the edge) increases the energy of the m=1, n=-1 MHD mode, decreases the energy of the other m=1 harmonics and paces the intermittency of the sawtooth (though the on-axis safety factor still oscillates around q=1). However, the amount of MP% necessary to interact with the tokamak helical states is lower than the corresponding one for the RFP, with an analogous lower intensity of magnetic fluctuations: this difference is related to the much stronger magnetic flux with

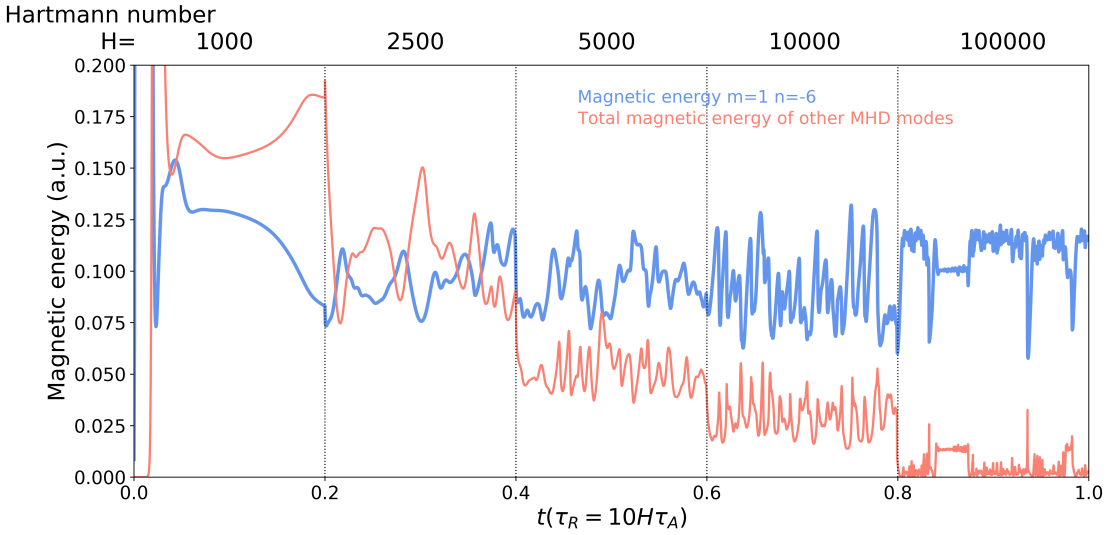

Figure 4. In 3D nonlinear MHD simulations quasi helical states with a chosen helical twist ($h = 6$ in this case) can emerge only with MP and at low dissipation. This explains the experimental observation from RFP experiments: there, QSH are observed only when plasma current is increased. In this simulation S and M vary, with constant $P = S/M = 10^2$. We also have $S = P^{1/2}H = 10H$.

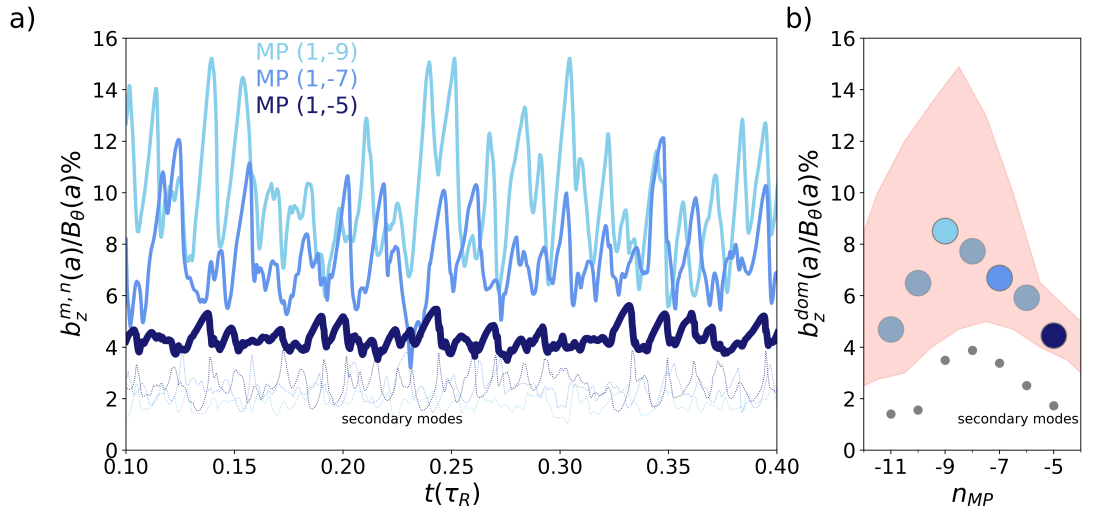

Figure 5. Magnetic Perturbations are a powerful tool to interact with QSH plasmas, i.e. the ones in the low dissipation regime of Fig. 2. In panel a) we show that we can use MPs with different helicities to direct the self-organization towards a helical state with the same helical twist as the edge MP. In panel b) we show that more quiescent states can be obtained using low-n MPs with m=1, corresponding to non-resonant helical regimes. Simulations with $S = 10^5, M = 10^3$.

respect to the plasma corrent in tokamaks with respect to RFPs.

3.6. Scaling of the "sawtoothing" characteristic time

We dub the characteristic time for both the sawtoothing dynamics of tokamaks and RFPs τ_{saw}, and we compute it by looking for the time intervals between maxima of selected physical quantities, like the magnetic energy associated to the m=1,n=-1 mode for the tokamak simulations (see the pictorial definition in the top-right panel of Fig. 6) or the value of $q(a)$ for the RFP simulations. We define τ_{saw} as the average of the time intervals in a single simulation and we compute the related error $\delta_{\tau_{saw}}$.

For the tokamak configuration we have analyzed a database of simulations with $10^4 < S < 10^7$ and $10^3 < M < 10^6$. We then look for a scaling $\tau_{saw} \propto S^\alpha M^\beta$, which gives $\alpha = 0.58 \pm 0.01$, $\beta = -0.26 \pm 0.03$. An analogous scaling can be obtained considering a different couple of visco-resistive dissipation parameters, meaning the couple (H, P): noting that in the

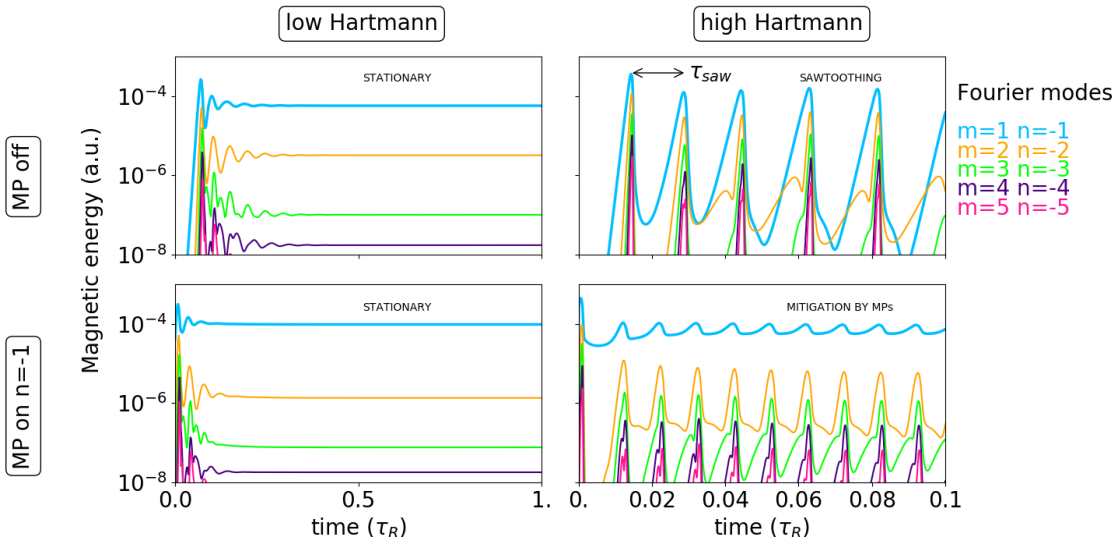

Figure 6. Solutions of the 3D nonlinear MHD model for tokamak cases. A clear analogy can be drawn with Fig. 2 regarding the dynamical features of the simulations: high Hartmann favors sawtoothing, which can be in turn tamed by proper MPs.

rescaled equations time is transformed according to Eq. 2 ($\tau \rightarrow \bar{\tau}_{saw} = P^{-\frac{1}{2}}\tau$), this scaling can be analyzed provided that the value of τ_{saw} is rescaled as well. We can thus obtain a new scaling which is linked to the previous one by a simple relation obtained by substituting the definitions of (H, P) in terms of (S, M), i.e. $\bar{\tau}_{saw} \propto H^{\alpha+\beta} P^{\frac{1}{2}(\alpha-\beta-1)}$. The advantage of this choice of parameters is that it yields a clear scaling of the rescaled sawtoothing period as $\bar{\tau}_{saw} \propto H^{0.32\pm0.03} P^{-0.07\pm0.02}$ which depends mostly on H, see the blue dots of Fig. 7. Previous work about the characterization of the sawtoothing repetition time is available: in [65] a different MHD model is used, indicating a scaling $\tau_{saw-Vlad1991} \propto S^{0.45} M^{-0.20}$, compatible with the scaling from SpeCyl simulations; strong dependence on the perpendicular thermal diffusivity and on the edge safety factor is also found. Another result consistent with our computation can be found in [66], where a scaling $\tau_{saw-McGuire1979} \propto S^{0.40}$ is given. Some work on sawtoothing in current-carrying hybrid tokamak-stellarator devices is found in [67], where the dependence on the safety factor only is described.

Let us now consider the "sawtoothing" repetition time in our database of RFP simulations (the same one used for the statistical analysis of Sec. 3.2). We compute τ_{saw} only for simulations showing an intermittent behaviour, i.e. with Hartmann $H > H_c \sim 3 \cdot 10^3$. From the whole database we obtain a scaling $\tau_{saw} \propto S^{0.91\pm0.03} M^{-0.07\pm0.07}$. Considering the rescaled sawtoothing characteristic period we easily obtain $\bar{\tau}_{saw} \propto H^{0.84\pm0.07} P^{-0.01\pm0.04}$, again showing a clear dependence on the Hartmann number only.
Quantitative differences are observed between the two

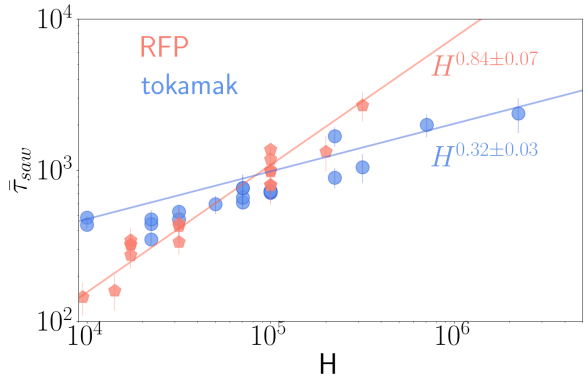

Figure 7. Scaling of the rescaled sawtoothing characteristic time $\bar{\tau}_{saw}$ with the Hartmann number. RFP simulation are colored in salmon, while tokamak ones in blue.

magnetic configurations under scrutiny: in particular the increase of the sawtoothing time when decreasing visco-resistive dissipation is much faster in the RFP than in the tokamak, $H^{0.84}$ in the RFP, while $H^{0.32}$ in the tokamak. The relatively strong dependence of τ_{saw} on dissipation, already found in [21], may explain why RFP quasi-helical states are observed to become more persistent (i.e. with less sawtoothing events) when increasing current (i.e. decreasing resistivity): in Fig.5a of [49] a strong dependence of QSH-persistence is in fact observed with the Lundquist number, which in turn strongly depends on plasma current.

4. Topology of quasi-helical states: barriers to the transport of magnetic field lines

In this section we show that a suitable choice of the MP spectrum at the edge is an important ingredient for the attainment of higher magnetic order. We focus on several aspects of the magnetic field topology all along two RFP simulations. We discuss Poincaré plots, Lagrangian Coherent Structures (LCS) computation and connection length L_c. The studies presented in this work are performed with the NEMATO field line tracing code (presented in [68] and numerically benchmarked in [69]). Few preliminary words about the LCS technique: it is borrowed from the study of dynamical systems, can be used to distinguish regions with different transport qualities. The most important feature of LCSs is that, for a meaningful finite time span which characterizes a LCS [16], magnetic field lines belonging to different regions cannot mix with each other. The LCS technique allows a more refined analysis than a simple inspection of a Poincaré map. As shown in [70, 12], when a Poincaré map suggests only a stochastic behaviour, the LCS tool highlights some structures, which we color in blue in the panels a)-f) of Fig. 9. Moreover, LCSs can be used also in situations where a Poincaré plot can't be computed, i.e. in non-periodical flows [71, 72].

In the following we discuss the "degree" of magnetic order. Specifically, looking at Fig. 8 panel a), we define the degree of magnetic order to be high if there is a large area of the Poincaré plot occupied by conserved magnetic surfaces or, looking at Fig. 9, if we compute the presence of well-defined bundles of LCS (plotted in red), or if we measure a large connection length of magnetic field lines to the edge (white areas of high connection length maps on the poloidal sections, plotted in Fig. 9) and if such positive features resist to the sawtoothing events.

4.1. Poincaré plots of quasi-helical states

The two simulation cases that we consider differ only with respect to the dominant MHD mode, either a QSH state with a non-resonant $m_{MP} = 1, n_{MP} = -6$ helical twist in the first row or a $m_{MP} = 1, n_{MP} = -7$ case in the second, in both cases with amplitude MP%= 2%. The visco-resistive parameters of the simulations are $S = 10^6$, $M = 10^4$. In each case we study a dynamic cycle starting with the formation of a QSH state (first column of Fig. 8), continuing with a full development of the helical state (second column) and ending with a relaxation of the quasi-helical fields, resulting in the loss of part of the positive helical magnetic topology features, as can be seen by the generalized reduction of the area occupied by conserved magnetic surfaces in the third column of Fig. 8. Poincaré plots of Fig. 8 are performed on a toroidal surface of section. In the first row the $m_{MP} = 1, n_{MP} = -6$ simulation case, in the second row the $m_{MP} = 1, n_{MP} = -7$ case. Fig. 8a shows a core region of conserved magnetic surfaces is present when the QSH state is forming (green region in the first row, orange in the second). Surrounding the core is a stochastic region, whose radial extension depends on the relative intensity of the dominant helical mode and its perturbations (grey region). An edge region with conserved surfaces, related to the $m \sim 0$ character of the edge, is a feature observed in all the RFPs and providing a barrier to transport [73, 74].

As a first consideration we notice that the area of conserved magnetic surfaces in the non-resonant case is higher than that in the resonant case, both during the formation of the helical state and its relaxation to a Multiple Helicity state (last column of Fig. 8): this was already found in [12], but here the greater resilience to magnetic chaos is confirmed during the whole cycle of evolution of a QSH state. The last row of Fig. 8 depicts the profile of the helical safety factor: it is interesting to notice that a region of flat $q(\rho)$ is present only in resonant cases, and that its maximum extension encloses the conserved orange regions in panels d) and e) (see dotted pink lines). Another difference between the first two rows is that in resonant cases the core-conserved region does not enclose the cylindrical axis at $r/a = 0$, while the non-resonant cases generally do (apart from the relaxation phase). This may be important for understanding the features of the electron temperature profiles measured in RFP experiments, which display clear internal transport barriers previously put in relation to magnetic chaos healing and helical q profile [75, 76].

In the following, we consider the features of Lagrangian Coherent Structures, LCS, and of the connection length, L_c, during the magnetic field evolution.

4.2. Lagrangian Coherent Structures in quasi-helical states

Let us now consider the LCSs computed in the two cycles of QSH states, colored in red in Fig. 9. We considered just the LCS located in the core, i.e. at $r/a < 0.7$. LCS are computed using a finite time L_z of 4 toroidal turns for each magnetic field line. The particular choice of the finite time is the result of a compromise specific to each magnetic configuration analyzed. Too short an L_z ($L_z \ll L_k, L_{corr}$, with L_k the average Kolmogorov length of the system and L_{corr} the correlation length see Sec. VI of [69]) prevents LCSs to be computed because magnetic field lines are not followed long enough to put in evidence regions of fast separation, but allows for shorter computational

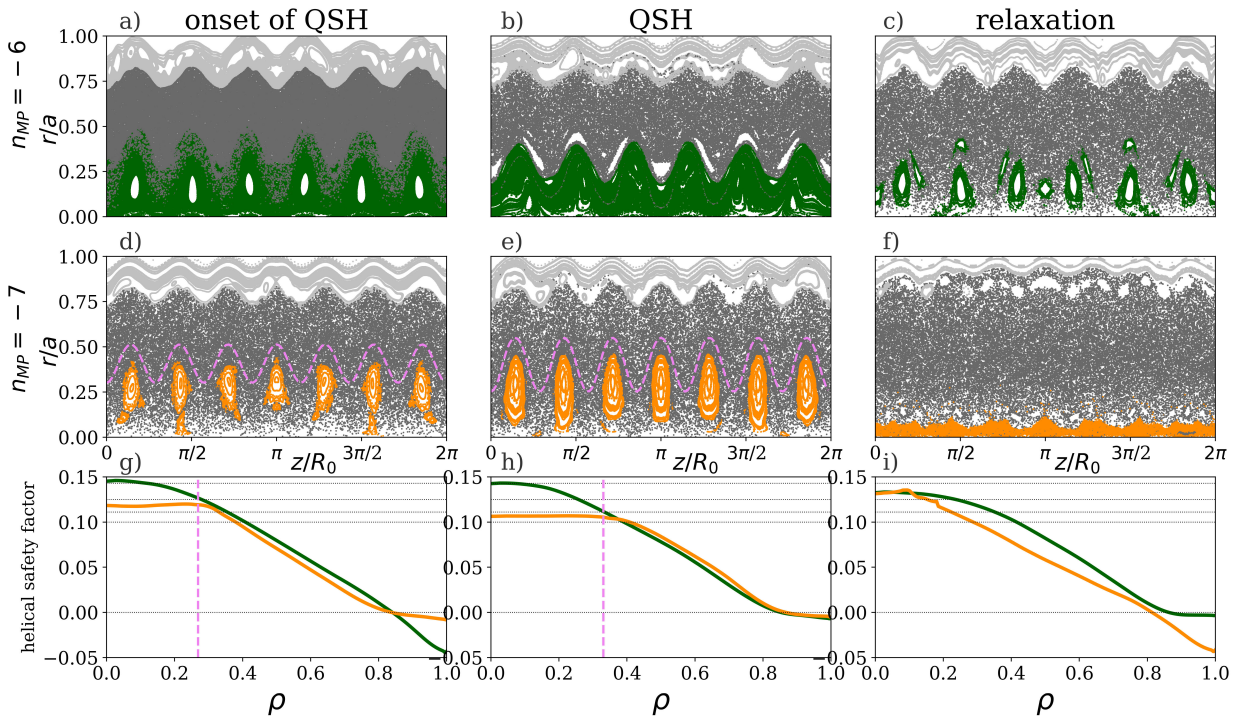

Figure 8. Magnetic topology in terms of Poincaré plots on a toroidal surface of section during the formation of a helical state, and its relation with the helical safety-factor. In the first line the evolution of magnetic field topology during a cycle of formation/breakdown of a non-resonant QSH state with $n_{MP} = -6$ is shown, while the second line shows a resonant QSH state with $n_{MP} = -7$. In the third line the helical safety factor for the different cases is shown, and one can notice the reversed-shear typical of resonant helical states. Safety factor is plotted against a "helical radius" ρ related to the volume contained inside nested helical flux surfaces. The dashed helical flux surfaces in plots of the second line correspond to the end of the flat safety factor region in the resonant case.

time; too high an L_z ($L_z \gg L_k, L_{corr}$) prevents LCSs to be computed because magnetic field lines in a finite domain decorrelate hiding the regions of fast separation. Considering a test-particle with the mass of an electron at a temperature of 700eV (typical of the RFX-mod experiments) travelling with thermal speed the chosen L_z corresponds to around 10 Alfvèn times, i.e. 10^{-6} s.

From a topological point of view there are no relevant differences between the LCSs' shape in the two quasi-helical states: they tend to encompass the helical core as it widens during the evolution of the helical state. A certain degree of difference can be observed in the presence of more developed bundles of LCSs in the non-resonant case, panels a)-c) than in the resonant case. Interestingly, in the latter case the position of a bundle of LCSs can be correlated with the position of reversed shear of the helical safety factor profile (see Fig. 8 and Ref.[75]).

LCSs are observed to evolve on a time scale slower than the dynamical one, as their shape does not change significantly between the beginning and the middle of QSH states in the first two columns of Fig. 9), which are separated by $\tau_{dyn} \sim 10^4\ \tau_A$. Another important time scale is the one related to the LCSs' power of separating different spatial regions, which lies on a shorter timescale $\tau_{sep} \sim 10^3\ \tau_A$ [12], after which LCSs become leaky.

An assumption at the basis of our use of the LCS technique is that the magnetic field line are used a proxy for the particle trajectories along the lines. It is our plan to use tools beyond this ansatz to take into account the behaviour of charged particle in the magnetic field under scrutiny, like the one described in Ref. [77].

A complete study of LCSs confinement properties and their relation to the mechanism of formation of Internal Transport Barriers (ITBs) in experiments (following previous studies in [78, 79]) will be presented in the future.

4.3. Study of the connection length to the edge

An important issue related to LCSs is how much these structures can confine magnetic field lines. To quantify the magnetic field lines confinement properties of LCSs, which can't be argued from a Poincaré plot, as a first step we compute the connection length to the edge, i.e. we measure the length L_c that a magnetic field line starting at (r_0, θ_0) covers to reach an edge radius

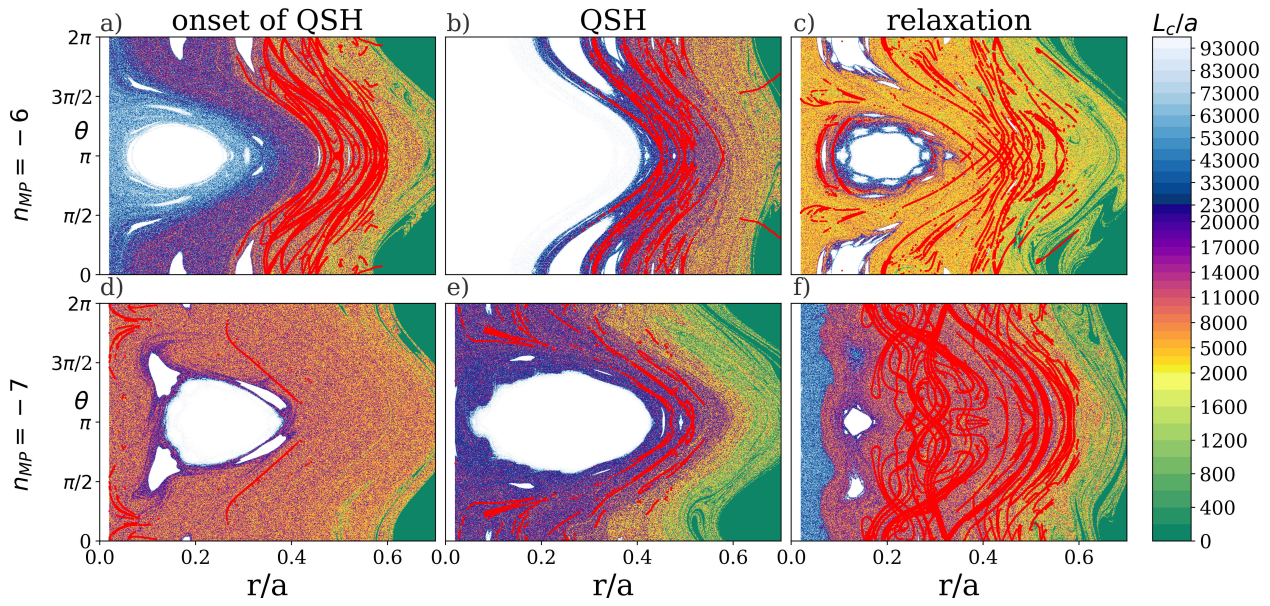

Figure 9. Red Lagrangian Coherent Structures (LCS) are superimposed to the contour plot of connection length of magnetic field lines to the edge. LCS are common feature of quasi-helical regimes, and are typically found in bundles. White levels of the contour plot correspond to the regions where $L_c = L_{c,max} = 10^5$. The red LCSs divide regions with different connection length, highlighting their role in creating and internal barrier to the transport of magnetic field lines.

taken as a reference for the computation $r/a = 0.75$. The results are shown in Fig. 9, where magnetic field lines have been integrated until a maximum normalized length of $L_{c,max} = 10^5$ (corresponding to a time of $\tau_{conn} \sim 10^5\ \tau_A$, i.e. much greater than the duration of a QSH cycle). We observe first that the areas in white, characterized by $L_c = L_{c,max}$, are generally larger in non-resonant states. We also notice regions where the connection length drops sharply: these regions are in good correspondence with the presence of bundles of LCS, another evidence of their role in defining special regions for the transport of magnetic field lines. We also note that when the ordering role of the helical mode fades, in the third column of Fig. 9, a rich set of topological structures appear connecting the plasma core to the plasma edge with relatively low connection length. Consider for example the green spots at $r \sim 0.2, \theta \sim 0$ in panel c), which are named "escape channels" in plasma literature [80, 81]: there, they are shown to possess a rich fractal structure which may explain some anomalous values of transport coefficients in the plasma edge.

As a final point it is important to notice that a "barrier" structure persists even during the reconnection event (see panels c) and f)). The detailed impact of these properties on temperature profiles are under study, both from the numerical and the experimental point of view: the use of a numerical code for the solution of the anisotropic heat transport equation [82, 83] will help determining whether LCSs are responsible for the high temperature gradients observed in correspondence of Internal Transport Barriers [84], and an analogous work is ongoing looking at RFX-mod experimental data.

5. Role of plasma flow in enhancing quasi-helical states

Plasma rotation is the topic of a vast literature, because toroidal velocities of tens of km/s are measured both in tokamaks and RFPs, also in the absence of direct external momentum input. Among other things, rotation is involved in a mechanism of reduction of turbulent fluctuations of the magnetic field [85]. We refer the reader to [86] for an excellent and complete review of this subject.

In this section we describe a preliminary assessment of the interaction between a mean plasma flow and the helical self-organization process in RFPs. We performed a set of simulations with $S = 10^5$ and $M = 10^2$, imposing a MP on the $(1, -7)$ MHD mode with amplitude MP%= 2%; simulations of this kind are located in the top-right corner of the diagram of Fig. 2, corresponding to the ones with a more experimental-like dynamics of the magnetic field. The parameter which measure the dimensionless ad-hoc momentum source, S_M with respect to the dimensionless viscosity ν, $\frac{S_M}{\nu}$ is varied in the range $-7 \cdot 10^{-2} < \frac{S_M}{\nu} < 7 \cdot 10^{-2}$, corresponding to an initial maximum velocity of $-1.75 \cdot 10^{-2} < v_z^{0,0} < 1.75 \cdot 10^{-2}$.

As a preliminary result of this study we observe in Fig. 10a) that a moderate intensity of imposed axial flow

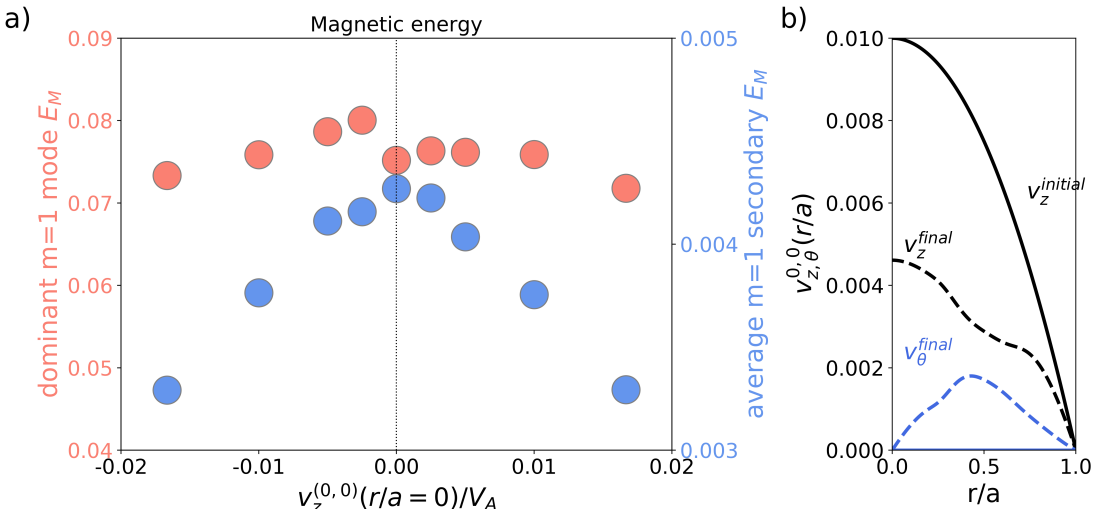

Figure 10. Panel a): addition of external momentum source increases the ratio between dominant and secondary perturbations. Panel b): the quasi-helical magnetic field interacts with the mean plasma flow by braking it, from its initial equilibrium parabolic profile (see Sec.2.1) to the final blue radial profiles.

(few percent of the Alfvèn speed, $v_A \sim 5000$ km/s in RFX-mod) leads to an enhancement of the helical state, in form of a modest increase of the energy associated to the dominant mode together with a clear decrease of the energy of secondary perturbations, even in the experimentally relevant region $v_z^{(0,0)}/v_A < 0.01$ (the ratio between the two quantities increases of around 25% with these simulation parameters), independent on the direction of the mean flow. It is also interesting to note that when a global quasi-helical state is established the main mechanism of interaction between magnetic and velocity field is rotation braking. Fig. 10b) shows the radial profile of the plasma flow $m = 0, n = 0$ components at the beginning (solid line) and at the end (dashed line) of the simulation with $\frac{S_M}{\nu} = 4 \cdot 10^{-2}$ (corresponding to an initial velocity $v_z^{(0,0)}(t = 0) = 10^{-2}$): one notices the strong damping of the $\hat{z}$ component of the velocity by the magnetic field, which is in part converted in a $\hat{\theta}$ component. The mechanisms behind this interaction are still under scrutiny.

The expected positive implications on magnetic field topology have not been studied yet, and will be the subject of a dedicated work.

6. Summary and final remarks

In this paper we discussed helical self-organization in current-carrying toroidal pinches for the magnetic confinement of fusion plasmas, in the framework of 3D nonlinear visco-resistive MHD modelling.

Two quantities rule the nature of helical states and the possibility to interact constructively with self-organization, namely plasma dissipation (Hartmann number H, the inverse product of resistivity and viscosity) and helical magnetic boundary conditions (with chosen intensity and helical twist). A complete picture of the role of these two quantities in featuring helical solutions has been given. Such a complete picture can be summarized in some ideas listed below.

First, there are only two combinations of Hartmann number and helical boundary conditions leading to quasi-helical solutions for the RFP: the solutions at high H, previously connected to experimental results in RFX-mod [26, 12], and the stationary helical solutions at low H , still lacking experimental evidence.

Second, it is possible to interact constructively with a helically self-organized RFP plasma, by lowering dissipation (i.e. by increasing plasma current in the experiment) and favoring a selected MHD mode by modulating appropriately the edge magnetic field (i.e. by acting on the plasma-edge with a control system). The fact that a non-resonant helical twist at the edge can induce a more quiescent dynamics in place of a sawtoothing one is a positive feature of high H states, whose exploration already successfully started in RFX-mod device [12].

Third, the study of the RFP configuration can be extended to basic tokamak simulations with the same model: there, sawtoothing behaviour emerges at low dissipation too, also mitigated by imposing a small edge magnetic field at the boundary. Though this modelling does not pertain to advanced tokamak regimes and significant work is needed to further improve the predictive capability of numerical tools (toroidal geometry, finite β effects and the self-consistent evolution of plasma resistivity through

Spitzer's law just to mention the first physical effects that we're going to integrate in our modelling tools), we deem the similarities between tokamak and RFP helical states useful to deepen the understanding of basic behaviour of the internal kink mode [87, 61].
Fourth, the sawtoothing period in the simulations described in this paper is shown to depend on the Hartmann number only, i.e. on the simple product of resistivity and viscosity for both tokamaks and RFPs, a result to be validated experimentally.
In the second part of the paper the magnetic chaos healing phase associated with the formation of a quasi-helical state is tackled, highlighting the special role of low magnetic shear regions in helical states built upon resonant MHD modes and showing that non-resonant helical states have generally larger areas of conserved magnetic surfaces, embracing the geometrical axis of the configuration. It is presented for the first time the evolution of bundles of Lagrangian Coherent Structures responsible for the confinement of magnetic field lines close to the core of the helical plasma. LCSs surround the core of helical states and resist to the sawtoothing events in RFPs, even when magnetic topology gets less ordered. They are correlated to sharp gradients in the connection length of magnetic field lines to the edge, a fact that further supports the LCSs' role in the formation of internal transport barriers. In the future, an analysis of heat transport taking into account the strong anisotropy in the thermal conductivity of fusion plasmas and the presence of magnetic islands and stochastic magnetic fields is foreseen (using the tools described in Ref.[82, 83]), aiming at clarifying the role of LCS in sustaining transport barriers evolution - following previous studies [79, 88] and in the addition to already established mechanisms of microturbulence suppression caused by sheared flows [89, 90].
A further novel result presented in this work is that the positive interaction between edge MPs and the self-organized plasma can be enhanced by a macroscopic plasma rotation: a clear energy separation between dominant helical mode and secondary fluctuations emerges, leading to possible enhancements in the dynamics and topology of helical states.
Future numerical work will be dedicated to analyze the role of a finite pressure gradient and to the effect of a realistic boundary on the helical self-organization of the RFP, adding a thin resistive shell and a vacuum layer between the plasma and the ideal shell where MPs are applied. Another area of future work is related to the self-consistent evolution of plasma resistivity and viscosity through the solution of heat transport equation with the PIXIE3D code [32]. Experimental activity to validate our numerical results is planned in the upgraded RFX-mod2 machine [91], both regarding the topic of transport barriers formation and the topic of interaction between helical states and plasma flow.

7. Acknowledgments

We thank L. Chacón for many helpful interactions regarding the NEMATO code, P. Scarin and G. Spizzo for useful discussions about magnetic field topology and transport coefficients. We thank M.E. Puiatti for the careful reading of the manuscript. We also thank the whole RFX-mod team. The authors acknowledge use of the computational resources provided by the EUROfusion High Performance Computer (Marconi-Fusion) through the EUROfusion project named "PIXIE3D", which includes the topological studies described in Sec. 4.

Appendix A. Viscosity and resistivity in plasma fluid theory

The aim of this appendix is to define few quantities - resistivity, viscosity, adimensional resistive and viscous Lundquist number, Hartmann number - in the framework of plasma fluid theory and in terms of measurable plasma parameters.
Nor the steps involved in the construction of a single fluid theory from kinetic theory, nor the mathematics involved in fluid equations closure will be explained here. We refer to [92] for an explanation of the steps involved in the construction of a single fluid theory from kinetic theory, and of the mathematics involved in fluid equations closure.
A Chapman-Enskog two-Laguerre-polynomial closure scheme in the case of a magnetized plasma (a magnetized plasma is defined by $\Omega_i\tau_{ii}, \Omega_e\tau_{ee} \gg 1$ i.e. meaning that the ion Larmor radius is much smaller than a characteristic length-scale. $\Omega_{i,e} = \frac{eB}{m_{i,e}}$ is the ion/electron cyclotron frequency) yields the following expressions for resistivity and viscosity perpendicular to the magnetic field:

$$\eta = \frac{m_e}{n_e e^2 \tau_{ei}} = \frac{0.12}{\pi^{3/2}} \frac{m_e^{1/2} e^2}{\epsilon_0^2} \frac{Z \ln\Lambda}{T_e^{3/2}} \tag{A.1}$$

$$\mu_\perp = \frac{3}{2} \frac{n_i T_i}{\Omega_i^2 \tau_{ii}}$$
$$= \frac{1}{8\pi^{3/2}} \frac{m_p^{3/2} e^2}{\epsilon_0^2} \frac{n_e^2 \gamma^{3/2} \ln\Lambda}{B^2 T_i^{1/2}} \tag{A.2}$$

with τ_{ii}, τ_{ei} representing the average time between an ion-ion, electron-ion collision, Λ the Coulomb logarithm, $T_{i,e}$ the ion/electron temperatures measured in eV, Ze is the plasma ions electric charge, $n_{i,e}$ is the ion/electron particles density, γ is the ratio between ion and proton mass.
From these definitions and the definition of Alfvèn time

$\tau_A = \frac{a\sqrt{\mu_0 n_i \gamma m_p}}{B}$ one can then define the resistive and viscous Lundquist numbers:

$$S = \frac{\mu_0 a v_A}{\eta} = \frac{\pi^{3/2}}{0.12} \frac{\mu_0^{1/2}\epsilon_0^2}{m_p^{1/2} m_e^{1/2} e^2} \frac{aBT_e^{3/2}}{\gamma^{1/2} n_e^{1/2} Z^{1/2} \ln\Lambda} \quad \text{(A.3)}$$

$$M_\perp = \frac{a v_A \rho_0}{\mu_\perp} = 44.5 \frac{\epsilon_0^2}{\mu_0^{1/2} m_p e^2} \frac{aB^3 T_i^{1/2}}{\gamma n_e^{3/2} Z^{1/2} \ln\Lambda}. \quad \text{(A.4)}$$

From these definitions one can estimate the perpendicular Hartmann number:

$$H_\perp = (SM_\perp)^{1/2} = 45.4 \frac{\epsilon_0^2}{m_p^{3/4} m_e^{1/4} e^2} \frac{aB^2 T_e^{3/4} T_i^{1/4}}{\gamma^{3/4} n_e Z^{1/2} \ln\Lambda}, \quad \text{(A.5)}$$

we get the simplified relation $H \propto Tn^{-1}$ used in Sec. 3.3.

References

[1] J. Wesson. *Tokamaks*. Clarendon Press, Oxford, second edition, 1997.

[2] P. Buratti, M. Baruzzo, R.J. Buttery, C.D. Challis, I.T. Chapman, F. Crisanti, L. Figini, M. Gryaznevich, T.C. Hender, D.F. Howell, H. Han, F. Imbeaux, E. Joffrin, J. Hobirk, O.J. Kwon, X. Litaudon, J. Mailloux, and JET-EFDA contributors. Kink instabilities in high-beta jet advanced scenarios. *Nuclear Fusion*, 52(2):023006, 2012.

[3] A. Weller, A. D. Cheetham, A. W. Edwards, R. D. Gill, A. Gondhalekar, R. S. Granetz, J. Snipes, and J. A. Wesson. Persistent density perturbations at rational- q surfaces following pellet injection in the Joint European Torus. *Phys. Rev. Lett.*, 59:2303–2306, Nov 1987.

[4] L. Delgado-Aparicio, L. Sugiyama, R. Granetz, D. A. Gates, J. E. Rice, M. L. Reinke, M. Bitter, E. Fredrickson, C. Gao, M. Greenwald, K. Hill, A. Hubbard, J. W. Hughes, E. Marmar, N. Pablant, Y. Podpaly, S. Scott, R. Wilson, S. Wolfe, and S. Wukitch. Formation and stability of impurity "snakes" in tokamak plasmas. *Phys. Rev. Lett.*, 110:065006, Feb 2013.

[5] *See Chapter 9. D.F. Escande. "What is a Reversed Field Pinch?". Pag. 247 in Rotation and Momentum Transport in Magnetized Plasmas, volume 2.* Patrick H Diamond, Xavier Garbet, Philippe Ghendrih, and Yanick Sarazin. World Scientific, 2014.

[6] S. Cappello and R. Paccagnella. In E. Sindoni, editor, *Proceedings of the Workshop on Theory of Fusion Plasmas, Varenna, Italy*, page 595. Compositori, Bologna, 1990.

[7] S. Cappello and R. Paccagnella. Nonlinear plasma evolution and sustainement in reversed-field pinches. *Physics of Fluids B*, 4:611, 1992.

[8] J.M. Finn, R. Nebel, and C. Bathke. Single and multiple helicity ohmic states in reversed-field pinches. *Physics of Fluids B*, 4:1262, 1992.

[9] D.F. Escande, R. Paccagnella, S. Cappello, C. Marchetto, and F. D'Angelo. Chaos healing by separatrix disappearance in Quasi Single Helicity states of the reversed-field pinch. *Physical Review Letters*, 85(15):3169, 2000.

[10] S. Cappello and D. F. Escande. Bifurcation in viscoresistive MHD: the Hartmann number and the reversed-field pinch. *Physical Review Letters*, 85(18):3838, 2000.

[11] M Veranda, D Bonfiglio, S Cappello, L Chacón, and D F Escande. Impact of helical boundary conditions on nonlinear 3D magnetohydrodynamic simulations of reversed-field pinch. *Plasma Physics and Controlled Fusion*, 55(7):074015, 2013.

[12] M. Veranda, D. Bonfiglio, S. Cappello, D.F. Escande, F. Auriemma, D. Borgogno, L. Chacón, A. Fassina, P. Franz, M. Gobbin, et al. Magnetohydrodynamics modelling successfully predicts new helical states in reversed-field pinch fusion plasmas. *Nuclear Fusion*, 57(11):116029, 2017.

[13] G. Haller and G. Yuan. Lagrangian coherent structures and mixing in two-dimensional turbulence. *Physica D: Nonlinear Phenomena*, 147(3):352–370, 2000.

[14] G. Haller. Lagrangian coherent structures. *Annual Review of Fluid Mechanics*, 47:137–162, 2015.

[15] F Pegoraro, D Bonfiglio, S Cappello, G Di Giannatale, M V Falessi, D Grasso, and M Veranda. Coherent magnetic structures in self-organized plasmas. *Plasma Physics and Controlled Fusion*, 61(4):044003, mar 2019.

[16] D. Borgogno, D. Grasso, F. Pegoraro, and T. J. Schep. Barriers in the transition to global chaos in collisionless magnetic reconnection. I. ridges of the finite time lyapunov exponent field. *Physics of Plasmas*, 18(10):–, 2011.

[17] D. Borgogno, D. Grasso, F. Pegoraro, and T. J. Schep. Barriers in the transition to global chaos in collisionless magnetic reconnection. II. Field line spectroscopy. *Physics of Plasmas*, 18(10):–, 2011.

[18] J.B. Taylor. Relaxation of toroidal plasma and generation of reversed magnetic fields. *Physical Review Letters*, 33(19):1139, 1974.

[19] J. B. Taylor. Relaxation and magnetic reconnection in plasmas. *Rev. Mod. Phys.*, 58:741–763, Jul 1986.

[20] J.P. Dahlburg, D. Montgomery, G.D. Doolen, and L. Turner. Driven, steady state RFP computations. *Journal of Plasma Physics*, 40(1):39, 1988.

[21] S. Cappello and D. Biskamp. Reconnection processes and scaling laws in reversed-field pinch magnetohydrodynamics. *Nuclear Fusion*, 36(5):571, 1996.

[22] D. Bonfiglio, S. Cappello, and D. F. Escande. Dominant electrostatic nature of the Reversed Field Pinch dynamo. *Phys. Rev. Lett.*, 94:145001, 2005.

[23] S. Cappello, D. Bonfiglio, D.F. Escande, S.C. Guo, I. Predebon, F. Sattin, M. Veranda, P. Zanca, C. Angioni, L. Chacón, J.Q. Dong, X. Garbet, and S.F. Liu. Equilibrium and transport for quasi-helical reversed-field pinches. *Nuclear Fusion*, 51(10):103012, 2011.

[24] S. C. Jardin, N. Ferraro, and I. Krebs. Self-organized stationary states of tokamaks. *Phys. Rev. Lett.*, 115:215001, Nov 2015.

[25] S. Cappello, D. Bonfiglio, D. F. Escande, S. C. Guo, A. Alfier, and R. Lorenzini RFX Team. The reversed-field pinch toward magnetic order: a genuine self-organization. *AIP Conference Proceedings*, 1069(1):27–39, 2008.

[26] D. Bonfiglio, M. Veranda, S. Cappello, D. F. Escande, and L. Chacón. Experimental-like helical self-organization in Reversed-Field Pinch modeling. *Phys. Rev. Lett.*, 111:085002, Aug 2013.

[27] P. Sonato, G. Chitarin, P. Zaccaria, F. Gnesotto, S. Ortolani, A. Buffa, M. Bagatin, W.R. Baker, S. Dal Bello, P. Fiorentin, L. Grando, G. Marchiori, D. Marcuzzi, A. Masiello, S. Peruzzo, N. Pomaro, and G. Serianni. Machine modification for active MHD control in RFX. *Fusion Engineering and Design*, 66:161, 2003.

[28] S.C. Prager, J. Adney, A. Almagri, J. Anderson, A. Blair, D.L. Brower, M. Cengher, B.E. Chapman, S. Choi, D. Craig, S. Combs, D.R. Demers, D.J. Den Hartog, B. Deng, W.X. Ding, F. Ebrahimi, D. Ennis, G. Fiksel, R. Fitzpatrick, C. Foust, C.B. Forest, P. Franz, L. Frassinetti, J. Goetz, D. Holly, B. Hudson, M. Kaufman, T. Lovell, L. Marrelli, P. Martin, K. McCollam, V.V. Mirnov, P. Nonn, R. O'Connell, S. Oliva, P. Piovesan, I. Predebon, J.S. Sarff, G. Spizzo, V. Svidzinski, M. Thomas, E. Uchimoto, R. White, and M. Wyman. Overview of results in the MST reversed field pinch experiment. *Nuclear Fusion*, 45(10):S276, 2005.

[29] W. Liu, T. Lan, W. Mao, H. Li, J. Xie, A. Liu, S. Wan, H. Wang, J. Zheng, X. Wen, H. Zhou, W. You, C. Li, W. Bai, C. Tu, M. Tan, B. Luo, C. Fu, F. Huang, H. Xu, T. Deng, J. Zhu, S. Zhang, Y. Adil, J. Hu, B. Xiao, Z. Luo, H. Wang, B. Shen, P. Fu, L. Yang, Y. Song, Q. Yang, J. Zheng, H. Xu, P. Zhang, C. Xiao, and W. Ding. Overview of Keda Torus eXperiment initial results. *Nuclear Fusion*, 57(11):116038, 2017.

[30] P. R Brunsell, H. Bergsåker, M. Cecconello, J. R. Drake, R. M. Gravestijn, A. Hedqvist, and J.-A. Malmberg. Initial results from the rebuilt EXTRAP t2r RFP device. *Plasma Physics and Controlled Fusion*, 43(11):1457–1470, oct 2001.

[31] S. Masamune, A. Sanpei, R. Ikezoe, T. Onchi, K. Murata, K. Oki, H. Shimazu, T. Yamashita, and H. Himura. Characterization of Initial Low-Aspect Ratio RFP plasmas in RELAX. *Journal of the Physical Society of Japan*, 76:123501, 2007.

[32] L. Chacón. An optimal, parallel, fully implicit Newton-Krylov solver for three-dimensional viscoresistive magnetohydrodynamics. *Physics of Plasmas*, 15:056103, 2008.

[33] D. Bonfiglio, L. Chacón, and S. Cappello. Nonlinear three-dimensional verification of the SpeCyl and PIXIE3D magnetohydrodynamics codes for fusion plasmas. *Physics of Plasmas*, 17:082501, 2010.

[34] S. Cappello. Bifurcation in the MHD behaviour of a self-organizing system: the reversed-field pinch (RFP). *Plasma Physics and Controlled Fusion*, 46(12B):B313, 2004.

[35] H.E. Stherblom, S. Mazur, and P. Nordlund. Resistivity profile effects in numerical magnetohydrodynamic simulations of the reversed-field pinch. *Plasma Physics and Controlled Fusion*, 38(12):2205, 1996.

[36] R. Fridström, B. E. Chapman, A. F. Almagri, L. Frassinetti, P. R. Brunsell, T. Nishizawa, and J. S. Sarff. Dependence of perpendicular viscosity on magnetic fluctuations in a stochastic topology. *Phys. Rev. Lett.*, 120:225002, May 2018.

[37] A. M. Futch, D. Craig, R. Hesse, and C. M. Jacobson. Role of resistivity and viscosity in the excitation of stable m=0 modes during the rfp sawtooth crash. *Physics of Plasmas*, 25(11):112506, 2018.

[38] M. Veranda, D. Bonfiglio, S. Cappello, and P. Scarin. Viscosity and resistivity in fluid

plasma theory: definition and scaling with plasma parameters. Technical report, Consorzio RFX, 2014.

[39] H. R. Strauss. The dynamo effect in fusion plasmas. *The Physics of Fluids*, 28(9):2786–2792, 1985.

[40] J. A. Holmes, B. A. Carreras, P. H. Diamond, and V. E. Lynch. Nonlinear dynamics of tearing modes in the reversed field pinch. *The Physics of Fluids*, 31(5):1166–1179, 1988.

[41] K. Kusano and T. Sato. Simulation study of the self-sustainment mechanism in the reversed-field pinch configuration. *Nuclear Fusion*, 30(10):2075, 1990.

[42] F. Ebrahimi, V. V. Mirnov, and S. C. Prager. Momentum transport from tearing modes with shear flow. *Physics of Plasmas*, 15(5), 2008.

[43] J.R. King, C.R. Sovinec, and V.V. Mirnov. First-order finite-larmor-radius fluid modeling of tearing and relaxation in a plasma pinch. *Physics of Plasmas*, 19:055905, 2012.

[44] M. Onofri, F. Malara, and P. Veltri. Compressibility effects in the dynamics of the reversed-field pinch. *Phys. Rev. Lett.*, 101:255002, Dec 2008.

[45] M. Onofri and F. Malara. Effects of the resistivity profile on the formation of a reversed configuration and single helicity states in compressible simulations of the reversed-field pinch. *Physics of Plasmas*, 20(10):102514, 2013.

[46] J. Scheffel and D.D. Schnack. Numerical studies of confinement scaling in the conventional reversed field pinch. *Nuclear Fusion*, 40(11):1885, 2000.

[47] G.L. Delzanno, L. Chacón, and J.M. Finn. Electrostatic mode associated with the pinch velocity in reversed-field pinch simulations. *Physics of Plasmas*, 15:122102, 2008.

[48] H. P. Furth, P. H. Rutherford, and H. Selberg. Tearing mode in the cylindrical tokamak. *The Physics of Fluids*, 16(7):1054–1063, 1973.

[49] P. Piovesan, M. Zuin, A. Alfier, D. Bonfiglio, F. Bonomo, A. Canton, S. Cappello, L. Carraro, R. Cavazzana, D.F. Escande, A. Fassina, M. Gobbin, R. Lorenzini, L. Marrelli, P. Martin, E. Martines, R. Pasqualotto, M.E. Puiatti, M. Spolaore, M. Valisa, N. Vianello, and P. Zanca. Magnetic order and confinement improvement in high-current regimes of RFX-mod with MHD feedback control. *Nuclear Fusion*, 49:085036, 2009.

[50] P. Piovesan, D. Bonfiglio, F. Bonomo, et al. Influence of external 3D magnetic fields on helical equilibrium and plasma flow in RFX-mod. *Plasma Physics and Controlled Fusion*, 53:084005, 2011.

[51] D. Bonfiglio, S. Cappello, D.F. Escande, G. Di Giannatale, A. Kryzhanovskyy, M. Veranda, L. Marrelli, and P. Zanca. Effect of a realistic boundary on the helical self-organization of the RFP. 2019. http://ocs.ciemat.es/EPS2019PAP/pdf/P1.1049.pdf.

[52] M.E. Puiatti, S. Dal Bello, L. Marrelli, P. Martin, P. Agostinetti, M. Agostini, V. Antoni, F. Auriemma, M. Barbisan, T. Barbui, M. Baruzzo, M. Battistella, F. Belli, P. Bettini, M. Bigi, R. Bilel, M. Boldrin, T. Bolzonella, D. Bonfiglio, M. Brombin, A. Buffa, A. Canton, S. Cappello, L. Carraro, R. Cavazzana, D. Cester, L. Chacon, B.E. Chapman, G. Chitarin, G. Ciaccio, W.A. Cooper, M. Dalla Palma, S. Deambrosis, R. Delogu, A. De Lorenzi, G. De Masi, J.Q. Dong, D.F. Escande, B. Esposito, A. Fassina, F Fellin, A. Ferro, C. Finotti, P. Franz, L. Frassinetti, M. Furno Palumbo, E. Gaio, F. Ghezzi, L. Giudicotti, F. Gnesotto, M. Gobbin, W.A. Gonzales, L. Grando, S.C. Guo, J.D. Hanson, S.P. Hirshman, P. Innocente, J.L. Jackson, S. Kiyama, M. Komm, L. Laguardia, C. Li, S.F. Liu, Y.Q. Liu, R. Lorenzini, T.C. Luce, A. Luchetta, A. Maistrello, G. Manduchi, D.K. Mansfield, G. Marchiori, N. Marconato, D. Marocco, D. Marcuzzi, E. Martines, S. Martini, G. Matsunaga, G. Mazzitelli, E. Miorin, B. Momo, M. Moresco, M. Okabayashi, E. Olofsson, R. Paccagnella, N. Patel, M. Pavei, S. Peruzzo, N. Pilan, L. Pigatto, R. Piovan, P. Piovesan, C. Piron, L. Piron, I. Predebon, C. Rea, M. Recchia, V. Rigato, A. Rizzolo, A.L. Roquemore, G. Rostagni, C Ruset, A. Ruzzon, L. Saja-Bohus, H. Sakakita, R. Sanchez, J.S. Sarff, E. Sartori, F. Sattin, A. Scaggion, P. Scarin, O. Schmitz, P. Sonato, E. Spada, S. Spagnolo, M. Spolaore, D.A. Spong, G. Spizzo, L. Stevanato, M. Takechi, C. Taliercio, D. Terranova, G.L. Trevisan, G. Urso, M. Valente, M. Valisa, M. Veranda, N. Vianello, G. Viesti, F. Villone, P. Vincenzi, N. Visona', Z.R. Wang, R.B. White, P. Xanthopoulos, X.Y. Xu, V. Yanovskiy, A. Zamengo, P. Zanca, B. Zaniol, L. Zanotto, E. Zilli, and M. Zuin. Overview of the RFX-mod contribution to the international fusion science program. *Nuclear Fusion*, 55(10):104012, 2015.

[53] Z.R. Wang and S.C. Guo. Physical understanding of the instability spectrum and the feedback control of resistive wall modes in reversed-field pinch. *Nuclear Fusion*, 51(5):053004, 2011.

[54] D. Bonfiglio, P. Martin, and P. Piovesan. Sawtooth control via n=1 applied magnetic perturbation in tokamak. 2013. http://ocs.ciemat.es/EPS2013PAP/pdf/P2.145.pdf.

[55] D. Bonfiglio, M. Veranda, S. Cappello, D.F.

Escande, and L. Chacón. Helical self-organization in 3D MHD modelling of fusion plasmas. *Plasma Physics and Controlled Fusion*, 57(4):044001, 2015.

[56] D. Bonfiglio, M. Veranda, S. Cappello, L. Chacón, and D.F. Escande. Sawtooth mitigation in 3D MHD tokamak modelling with applied magnetic perturbations. *Plasma Physics and Controlled Fusion*, 59(1):014032, nov 2016.

[57] F. Porcelli, D. Boucher, and M.N. Rosenbluth. Model for the sawtooth period and amplitude. *Plasma Physics and Controlled Fusion*, 38(12):2163–2186, dec 1996.

[58] B.V. Waddell, M.N. Rosenbluth, D.A. Monticello, and R.B. White. Non-linear growth of the m = 1 tearing mode. *Nuclear Fusion*, 16(3):528–532, jul 1976.

[59] R.E. Denton, J.F. Drake, R.G. Kleva, and D.A. Boyd. Skin currents and compound sawteeth in tokamaks. *Phys. Rev. Lett.*, 56:2477–2480, Jun 1986.

[60] F.D. Halpern, H. Lütjens, and J.F. Luciani. Diamagnetic thresholds for sawtooth cycling in tokamak plasmas. *Physics of Plasmas*, 18(10):102501, 2011.

[61] W. Shen and F. Porcelli. Linear and nonlinear simulations of the visco-resistive internal kink mode using the M3D code. *Nuclear Fusion*, 58(10):106035, aug 2018.

[62] O. Février, T. Nicolas, P. Maget, J.H. Ahn, X. Garbet, and H. Lutjens. Non-linear MHD simulations of sawteeth and their control by current and power depositions. *Nuclear Fusion*, 58(9):096008, jul 2018.

[63] M.F.F Nave, J Rapp, T Bolzonella, R Dux, M.J Mantsinen, R Budny, P Dumortier, M. von Hellermann, S Jachmich, H.R Koslowski, G Maddison, A Messiaen, P Monier-Garbet, J Ongena, M.E Puiatti, J Strachan, G Telesca, B Unterberg, M Valisa, P. de Vries, and contributors to the JET-EFDA Workprogramme. Role of sawtooth in avoiding impurity accumulation and maintaining good confinement in JET radiative mantle discharges. *Nuclear Fusion*, 43(10):1204–1213, sep 2003.

[64] V. Igochine, A. Gude, S. Günter, K. Lackner, Q. Yu, L. Barrera Orte, A. Bogomolov, I. Classen, R. M. McDermott, and N. C. Luhmann. Conversion of the dominantly ideal perturbations into a tearing mode after a sawtooth crash. *Physics of Plasmas*, 21(11):110702, 2014.

[65] G. Vlad, G. Bracco, and P. Buratti. Scaling of the sawtooth repetition time from simulations with reduced MHD equations, and comparison with experiments in the frascati tokamak. *Nuclear Fusion*, 31(8):1536–1540, aug 1991.

[66] K. McGuire and D.C. Robinsong. Sawtooth oscillations in a small tokamak. *Nuclear Fusion*, 19(4):505, 1979.

[67] N. A. Roberds, L. Guazzotto, J. D. Hanson, J. L. Herfindal, E. C. Howell, D. A. Maurer, and C. R. Sovinec. Simulations of sawtoothing in a current carrying stellarator. *Physics of Plasmas*, 23(9):092513, 2016.

[68] J.M. Finn and L. Chacón. Volume preserving integrators for solenoidal fields on a grid. *Physics of Plasmas*, 12, 2005.

[69] G. Ciaccio, M. Veranda, D. Bonfiglio, S. Cappello, G. Spizzo, L. Chacón, and R. B. White. Numerical verification of Orbit and Nemato codes for magnetic topology diagnosis. *Physics of Plasmas*, 20(6):062505, 2013.

[70] G Rubino, D Borgogno, M Veranda, D Bonfiglio, S Cappello, and D Grasso. Detection of magnetic barriers in a chaotic domain: first application of finite time lyapunov exponent method to a magnetic confinement configuration. *Plasma Physics and Controlled Fusion*, 57(8):085004, 2015.

[71] G. Di Giannatale, M. V. Falessi, D. Grasso, F. Pegoraro, and T. J. Schep. Coherent transport structures in magnetized plasmas. i. theory. *Physics of Plasmas*, 25(5):052306, 2018.

[72] G. Di Giannatale, M. V. Falessi, D. Grasso, F. Pegoraro, and T. J. Schep. Coherent transport structures in magnetized plasmas. ii. numerical results. *Physics of Plasmas*, 25(5):052307, 2018.

[73] G. Spizzo, S. Cappello, A. Cravotta, D.F. Escande, I. Predebon, L. Marrelli, P. Martin, and R.B. White. Transport barriers inside the reversal surface in the chaotic regime of the reversed-field pinch. *Physical Review Letters*, 96:025001, 2006.

[74] E. Martines, R. Lorenzini, B. Momo, S. Munaretto, P. Innocente, and M. Spolaore. The plasma boundary in single helical axis RFP plasmas. *Nuclear Fusion*, 50(3):035014, 2010.

[75] M. Gobbin, D. Bonfiglio, D. F. Escande, et al. Vanishing magnetic shear and electron transport barriers in the RFX-mod reversed-field pinch. *Phys. Rev. Lett.*, 106:025001, Jan 2011.

[76] R. Lorenzini, E. Martines, P. Piovesan, D. Terranova, P. Zanca, M. Zuin, A. Alfier, D. Bonfiglio, F. Bonomo, A. Canton, S. Cappello, L. Carraro, R. Cavazzana, D.F. Escande, A. Fassina,

P. Franz, M. Gobbin, P. Innocente, L. Marrelli, R. Pasqualotto, M.E. Puiatti, M. Spolaore, M. Valisa, N. Vianello, and P. Martin. Self organized helical equilibria as a new paradigm for ohmically heated fusion plasmas. *Nature Physics*, 5:570, 2009.

[77] R. B. White and M. S. Chance. Hamiltonian guiding center drift orbit calculation for plasmas of arbitrary cross section. *The Physics of Fluids*, 27(10):2455–2467, 1984.

[78] J.H. Misguich, J.D. Reuss, D. Constantinescu, G. Steinbrecher, M. Vlad, F. Spineanu, B. Weyssow, and R. Balescu. Noble cantor sets acting as partial internal transport barriers in fusion plasmas. *Plasma Phys. Control. Fusion*, 44:L29–L35, 2002.

[79] S. R. Hudson and J. Breslau. Temperature contours and ghost surfaces for chaotic magnetic Fields. *Phys. Rev. Lett.*, 100:095001, Mar 2008.

[80] R. L. Viana, E. C. Da Silva, T. Kroetz, I. L. Caldas, M. Roberto, and M. A. F. Sanjun. Fractal structures in nonlinear plasma physics. *Philosophical Transactions of the Royal Society A: Mathematical, Physical and Engineering Sciences*, 369(1935):371–395, 2011.

[81] A. Punjabi and A. Boozer. Homoclinic tangle in tokamak divertors. *Physics Letters A*, 378(32):2410 – 2416, 2014.

[82] D. del Castillo-Negrete and L. Chacón. Local and nonlocal parallel heat transport in general magnetic Fields. *Phys. Rev. Lett.*, 106:195004, May 2011.

[83] L. Chacón, D. del Castillo-Negrete, and C.D. Hauck. An asymptotic-preserving semi-lagrangian algorithm for the time-dependent anisotropic heat transport equation. *Journal of Computational Physics*, 272:719 – 746, 2014.

[84] M.E. Puiatti, M. Valisa, M. Agostini, F. Auriemma, F. Bonomo, L. Carraro, A. Fassina, M. Gobbin, R. Lorenzini, B. Momo, A. Scaggion, B. Zaniol, A. Alfier, L. Apolloni, M. Baruzzo, T. Bolzonella, D. Bonfiglio, A. Canton, S. Cappello, R. Cavazzana, S. Dal Bello, G. De Masi, D.F. Escande, P. Franz, E. Gazza, S. Guo, P. Innocente, G. Marchiori, L. Marrelli, P. Martin, E. Martines, S. Martini, S. Menmuir, L. Novello, R. Paccagnella, P. Piovesan, L. Piron, I. Predebon, A. Ruzzon, F. Sattin, P. Scarin, A. Soppelsa, G. Spizzo, S. Spagnolo, M. Spolaore, D. Terranova, M. Veranda, N. Vianello, P. Zanca, L. Zanotto, and M. Zuin. Internal and external electron transport barriers in the RFX-mod reversed-field pinch. *Nuclear Fusion*, 51(7):073038, 2011.

[85] P.H. Diamond, C.J. McDevitt, .D. Grcan, T.S. Hahm, W. X. Wang, E.S. Yoon, I. Holod, Z. Lin, V. Naulin, and R. Singh. Physics of non-diffusive turbulent transport of momentum and the origins of spontaneous rotation in tokamaks. *Nuclear Fusion*, 49(4):045002, 2009.

[86] V.D. Pustovitov. Integral torque balance in tokamaks. *Nuclear Fusion*, 51(1):013006, 2011.

[87] F. Porcelli. Viscous resistive magnetic reconnection. *The Physics of Fluids*, 30(6):1734–1742, 1987.

[88] D. del Castillo-Negrete and D. Blazevski. Modulated heat pulse propagation and partial transport barriers in chaotic magnetic fields. *Physics of Plasmas*, 23(4), 2016.

[89] J.W. Connor, T. Fukuda, X. Garbet, C. Gormezano, V. Mukhovatov, and M. Wakatani et. al. A review of internal transport barrier physics for steady-state operation of tokamaks. *Nuclear Fusion*, 44(4):R1, 2004.

[90] A. Fujisawa, K. Itoh, H. Iguchi, K. Matsuoka, S. Okamura, A. Shimizu, T. Minami, Y. Yoshimura, K. Nagaoka, C. Takahashi, M. Kojima, H. Nakano, S. Ohsima, S. Nishimura, M. Isobe, C. Suzuki, T Akiyama, K. Ida, K. Toi, S.-I. Itoh, and P. H. Diamond. Identification of zonal flows in a toroidal plasma. *Phys. Rev. Lett.*, 93:165002, Oct 2004.

[91] S. Peruzzo, M. Agostini, P. Agostinetti, M. Bernardi, P. Bettini, T. Bolzonella, A. Canton, L. Carraro, R. Cavazzana, S. Dal Bello, et al. Design concepts of machine upgrades for the RFX-mod experiment. *Fusion Engineering and Design*, 123:59–62, 2017.

[92] J.A. Bittencourt. *Fundamentals of plasma physics*. Springer, New York, 2004.